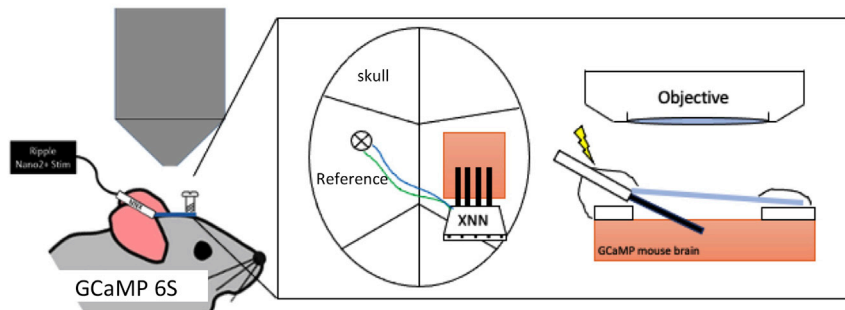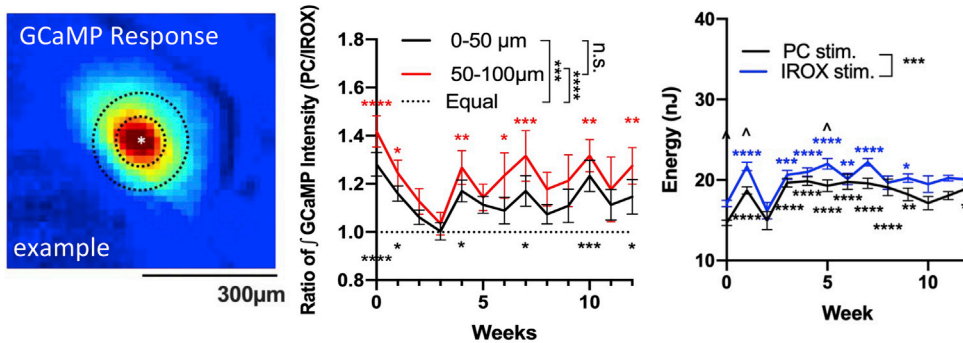**Article**

# Imaging the stability of chronic electrical microstimulation using electrodes coated with PEDOT/CNT and iridium oxide



Imaging chronic microstimulation stability and efficiency of PEDOT/CNT (PC) and IrOx coated electrodes in GCaMP6s mice

PEDOT/CNT is a more energy efficient material for chronic microstimulation than IrOx

Xin Sally Zheng,
Qianru Yang,
Alberto Vazquez,
Xinyan Tracy Cui

xic11@pitt.edu

### Highlights

Multimodal analyses reveal dynamic changes in stimulation efficiency and safety

PEDOT/CNT was more energy efficient compared to IrOx for chronic microstimulation

Abnormal cortical activity was elicited with paradigms commonly deemed as safe

## Article

# Imaging the stability of chronic electrical microstimulation using electrodes coated with PEDOT/CNT and iridium oxide

Xin Sally Zheng,[1] Qianru Yang,[1,2] Alberto Vazquez,[1,2,3,4] and Xinyan Tracy Cui[1,2,4,5,*]

## SUMMARY

**Chronic microstimulation is faced with challenges that require an additional understanding of stability and safety. We implanted silicon arrays coated with poly(3,4-ethylenedioxythiophene) (PEDOT)/Carbon Nanotubes (CNT), or PCand IrOx into the cortex of GCaMP6s mice and electrically stimulated them for up to 12 weeks. We quantified neuronal responses to stimulation using two-photon imaging and mesoscale fluorescence microscopy and characterized electrode performance over time. We observed dynamic changes in stimulation stability over time and a significant advantage in energy efficiency using PC coated electrodes over IrOx coated electrodes. In a subset of mice, we observed abnormal ictal cortical responses or cortical spreading depression using stimulation parameters commonly used in intracortical stimulation applications, suggesting the need to investigate the potential neuronal damage and redefine the stimulation safety limit. This study not only revealed the dynamic changes in stimulation efficiency after implantation but also reiterates the potential for PC as a high-efficiency material in chronic neuromodulation.**

## INTRODUCTION

Electrical microstimulation is a technique in which electrical currents are delivered through microelectrodes to excite the neuronal tissue. It not only serves as a valuable tool for researchers in the neuroscience community for dissecting neural circuits, relating brain regions, studying behaviors (Yeomans and Frankland, 1995; Tehovnik et al., 2004; Strick and Preston, 1978), but also an essential method for neuromodulation. Neuromodulation via electrical stimulation has partially restored vision (Schmidt et al., 1996), somatosensation (Flesher et al., 2016), hearing (McCreery et al., 2000), and has become a potential alternative or complement to conventional pharmaceuticals for the treatment of many chronic conditions such as asthma (Staats et al., 2018), diabetes (Daniels et al., 2010), and gastrointestinal disorders (Guo et al., 2019). The global market size for neural modulation is estimated to be USD 8.1 billion in 2019 and is estimated to grow by 13.1% by 2027(Global Neuromodulation Market Size study, 2020).

Safe and efficacious chronic electrical stimulation is faced with several challenges. First, to effectively stimulate a functional output, the delivered charge needs to be above the threshold charge density of the excitable tissue, yet below the charge injection limit to avoid irreversible redox reactions that could lead to tissue and electrode damage. In human neural prostheses applications, the threshold charge density ranges between 5 and 306 $\mu C/cm^2$ (1000-2000$\mu$s pulse width) for epi-retinal stimulation (Mahadevappa et al., 2005; Rizzo et al., 2003), and 190-2300 $\mu C/cm^2$ (200 $\mu$s pulse width) for intracortical visual stimulation (Hambrecht, 1995). Traditional stimulating electrode materials such as platinum with a charge injection limit of 50-150 $\mu C/cm^2$ (Rose and Robblee, 1990) cannot meet the full range of charge injection requirements for these applications, which drives the need for the development of high charge injection electrode materials. Second, the integrity of the implanted electrode faces unique challenges *in vivo* where the oxidative, corrosive, and dynamic environment accelerates material degradation (Kozai et al., 2015a; Prasad et al., 2012; Bullard et al., 2020; Caldwell et al., 2020). Material-related failure modes include fracture and delamination of the electrode insulation, corrosion, cracking, and delamination of electrode sites over the implantation duration. For stimulation applications, the failures in insulation will invite additional interstitial fluid under the existing insulation which can shunt the stimulating current, redistribute the current by effectively a larger surface, reducing the efficiency for precise neural activation. While inert metals

[1]Department of Bioengineering, University of Pittsburgh, 5057 Biomedical Science Tower 3, 3501 Fifth Avenue, Pittsburgh, PA 15260, USA

[2]Center for Neural Basis of Cognition, 115 Mellon Institute, 4400 Fifth Avenue, Pittsburgh, PA 15213, USA

[3]Department of Radiology, University of Pittsburgh, 200 Lothrop St, Pittsburgh, PA 15213, USA

[4]McGowan Institute for Regenerative Medicine, 3025 East Carson Street, Pittsburgh, PA 15219, USA

[5]Lead contact

*Correspondence: xic11@pitt.edu

https://doi.org/10.1016/j.isci. 2022.104539

such as platinum are considered resistant to corrosion, and iridium oxide has demonstrated a much higher charge injection limit (White and Gross, 1974; Cogan et al., 2004), both can degrade or detach from the substrate upon high charge injection or prolonged stimulation load (Cui and Zhou, 2007; Caldwell et al., 2020). Third, the implantation of the electrode devices inevitably triggers a foreign body response within the host tissue marked by the activation of microglia, breaching of the blood-brain barrier, and axonal degeneration. The existing host tissue inflammation due to electrode insertion can be exacerbated by electrical stimulation. There have been reports of electrical stimulation-induced vasoconstriction, thrombosis in venules and arterioles and blood-brain barrier breakdown within 30s of stimulation at a charge density threshold necessary for a sensorimotor response or for monophasic pulses at power densities greater than 0.5 mW/cm$^2$ (Pudenz et al., 1975a, 1975b; Mortimer et al., 1970). Moreover, electrochemical products as a result of faradaic charge injection have been reported to increase the presence of reactive oxygen species which severely damages myelin, impacting signal transduction in the neural network. (Chan et al., 1982) (Buettner, 1993; Chia et al., 1983; Griot et al., 1990; Konat and Wiggins, 1985; Sevanian, 1988). Furthermore, depending on the stimulation frequency, there may be persistent depression of neuronal excitability following stimulation of the cortex that lasts for several days following the cessation of the stimulation(McCreery et al., 1997).

The demand for stable and efficient neural interfaces drives the development of novel materials such as the conducting polymer coating PEDOT/CNT. Its nano-fibrous surface topography drastically increases the electrochemical surface area of its underlying substrate which results in much more efficient charge transfer compared to traditional metals. Our laboratory has previously demonstrated that PEDOT/CNTs electrochemically polymerized on platinum substrates resulted in a high charge injection limit of (2.5 mC/cm$^2$ using −0.6V as cathodic water window), high charge storage capacity (∼61.4 mC/cm$^2$), and low impedances at 1 kHz (3-7 kOhm). The PEDOT/CNT coating remained stable after three months of soaking in PBS with continuous electrical stimulation using biphasic pulses between weeks 5-7 at 0.35 mC/cm$^2$ at 50 Hz (Luo et al., 2011). *In vivo*, PEDOT/CNT coated electrodes showed significantly lower impedances while inducing significantly less neuronal death and inflammation compared to non-coated electrodes (Kolarcik et al., 2014).

Traditionally, the characterization of efficacious electrical stimulation has been based on *in vitro* testing (Kuramochi et al., 2006; Allahyari et al., 2016), histology (McCreery et al., 1988; Kolarcik et al., 2014), electrophysiology (Bent et al., 2019; Obien et al., 2015; Takahashi et al., 2019), and behavioral assays (King et al., 2019; Flesher et al., 2016). While these methods, respectively, provide unique information about the electrical stimulation, they do not allow for direct visualizations of the electrode-tissue interface. Modern imaging techniques and the rapidly developing genetic tools enable real-time observations of the electrode-tissue interface. Two-photon imaging and mesoscale fluorescent microscopy afford us single-cell and mesoscale interrogations of the brain, respectively. The ability to observe the interaction of the brain with the implanted devices has shed new light on understanding how different cellular players and anatomical features respond to electrical stimulation and the trauma induced by an implanted electrode device (Stieger et al., 2020; Eles and Kozai, 2020; Eles et al., 2018; Chen et al., 2021; Eles et al., 2017; Wellman and Kozai, 2018). (Kozai et al., 2012, 2016a; Welle et al., 2020; Xin et al., 2021).

The goal of this work is to investigate the longitudinal stimulation stability and efficiency of PEDOT/CNT compared to IrOx using multiple modalities of characterization including *in vivo* imaging, electrophysiology, and electrochemistry. We modified NeuroNexus planar arrays with PEDOT/CNT and IrOx, implanted them into the somatosensory cortex of GCaMP6s mice, and imaged cortical responses to electrical stimulation for up to 12 weeks. To assess the health of the neurons, we measured spontaneous electrophysiology before each stimulation session. To assess the stability of the implanted electrodes, we collected electrochemistry data. Results from this work will provide additional insight into the time course of the stability and efficiency of electrical stimulation using high-performing electrode materials.

## RESULTS

### Stability of stimulation efficiency and GCaMP response over 12 weeks

GCaMP mice were implanted with electrodes modified with PC and IrOx (Figure 1) Electrically evoked neuronal activity from the implanted electrodes was measured via GCaMP fluorescence changes through the cranial window over twelve weeks (Figure 2). To quantify the distance effect from the electrical stimulation, GCaMP responses of neural elements within 100 μm were divided into 0-50 μm and 50-100 μm bins.
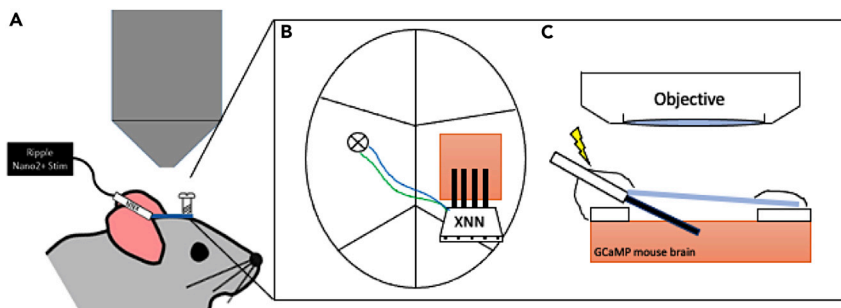
**Figure 1. Experimental setup**
(A) Illustration of a GCaMP6 mouse implanted with a Neuronexus (NNX) electrode, connected to a stimulator with a microscope objective above the head.
(B) Illustrated bird's eye view and (C) side view of the craniotomy. The electrode is implanted at a 30-degree- angle into the cortex, and the cranial window is sealed with a medical-grade elastomer and a clear cover glass. The electrode is cemented in place using dental acrylic. The reference and ground wires are shorted to a stainless-steel screw implanted in the contralateral hemisphere.

The mesoscale GCaMP responses in terms of maximum GCaMP intensity (Figure 3A) and integrated GCaMP intensities at distance bins 0-50 μm and 50-100 μm (Figure 3B and 3C) showed an overall corresponding increase to increasing stimulation amplitudes over time. The overall GCaMP response intensity (Figure 3a—C) was higher at early implantation periods (weeks 0, 1) relative to the sub-chronic implantation period (weeks 4, 5), and then showed a trend of recovery up to 12 weeks. Likewise, the mesoscale GCaMP response radius also increased with increasing stimulation amplitude. Different from trends observed with GCaMP response intensity, there was an overall lower GCaMP response radius at early implantation periods (weeks 0,1) but recovered by the sub-chronic implantation period (weeks 4,5) and remained relatively stable until week 12.

The longitudinal GCaMP responses were further analyzed to identify potential changes in the stability of the stimulation. GCaMP responses as a function of stimulation amplitude for each time point were fitted with linear regressions and we defined the stimulation efficiency to be the slopes of the fitting that showed p values less than 0.05. Neural activation efficiency represents the discrete recruitment of the neural population for incremental changes in stimulation amplitude. For neural elements within 50 μm of the implant, both electrode materials exhibited a significant decline in neuronal activation intensity efficiency beginning week 1 through week 6 for both materials accompanied by fluctuations and hints of recovery in weeks 7 through 12 for PC and IrOx-coated electrodes (Figure 4A). Neural elements within 50-100 μm of the center of the electrode exhibited overall lower neural activation efficiency compared to neural elements within 0-50 μm of the electrode. Additionally, there were significant declines in neuronal activation efficiency for both materials, beginning as early as week 1 for IrOx coated electrodes and week 2 for PC coated electrodes. However, unlike the 0-50 μm bin, PC coated electrode had a recovery in stimulation efficiency as early as week 6, whereas IrOx coated electrodes saw a continued decline in neuronal activation efficiency up to week 8 (Figure 4B). For both distance bins, there was no significant difference between material coating types for neuronal activation efficiency. Radius efficiency represents the discrete change in the extent of activation caused by incremental changes in stimulation amplitude. There was an overall significant change in radius efficiency over the study duration for both electrode materials. Both materials showed a trend of increase in efficiency over the study duration (Figure 4C). There was no significant difference between the two materials in recruiting additional neurons.

To compare the absolute GCaMP responses activated by both materials *in vivo*, we obtained the ratio of GCaMP responses activated by PC and IrOx coated electrodes. Ratios that are significantly higher than one indicate a significant advantage of PC-coated electrodes over IrOx electrodes in activating GCaMP responses. PC coated electrodes activated significantly higher GCaMP intensity within 0-50 μm of the center of the electrode at weeks 0, 1, 4, 7, 10, 12 compared to IrOx coated electrodes. Meanwhile, PC-coated electrodes activated significantly higher GCaMP intensity within 50-100 μm of the center of the electrode for weeks 0, 1, 4, 6, 7, 10, 12 (Figure 4D). Furthermore, PC coated electrodes stimulated larger radius of GCaMP responses compared to IrOx coated electrodes for weeks 0, 3, 4, 5, 6, 7, 10, 12 (Figure 4E).
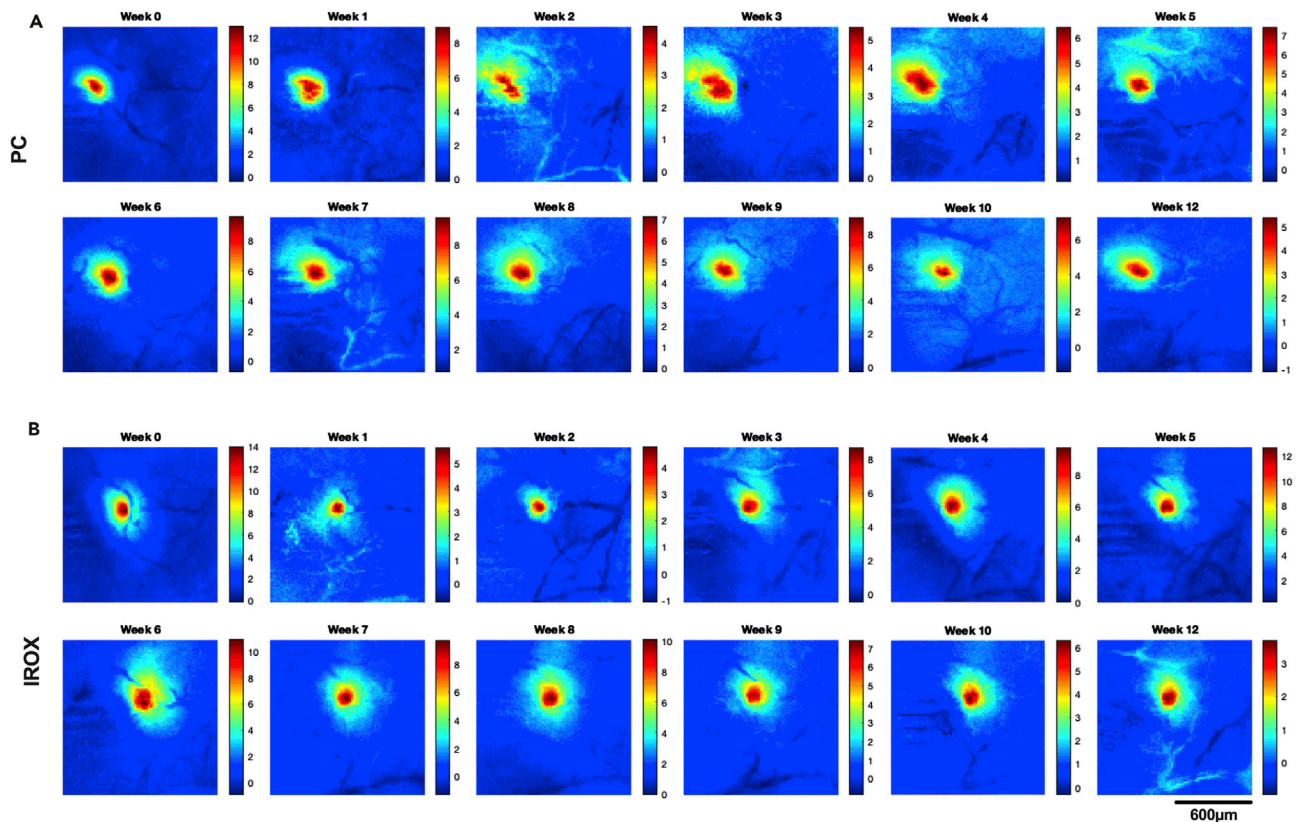
**Figure 2. GCaMP responses over time**
(A) Representative GCaMP responses to 30 μA stimulations from the same PC coated electrode site over 12 weeks.
(B) Representative GCaMP responses to 30 μA stimulations from the same IROX coated electrode site over 12 weeks. Color bars represent the *Z* score for each pixel. Scale bar represents 600 μm.

## Decrease in neuronal excitability over time

We performed electrical stimulations and imaged using two-photon microscopy (TPM) to gauge potential changes in neuronal excitability. Threshold maps of GCaMP responses showed a trend of increase over 7 weeks (Figures 5A–5F). We fitted the strength-duration curves of electrode sites that were observable with TPM for five mice and observed a qualitative increase in rheobase (Figure 5G) and a decrease in chronaxie (Figure 5H) from week one to week 7.

## Longitudinal electrophysiology and changes in electrode functions

We measured spontaneous spike signals before electrical stimulation to gauge the activity of the neurons nearby the electrode sites (Figures 6A and B). There was an overall significant change in single unit count per electrode for both materials. Additionally, there were significant decreases in single unit counts for both materials. Specifically, this was observed at weeks 4, 5, 6, 7, 8, 10 for PC coated electrodes and weeks 6, 8, 10, 11for IrOx coated electrodes (Figure 6C). Furthermore, there was an overall significant change in the amplitude of the largest unit recorded per array over the implant duration for both materials at week 5, and week 11 for IrOx (Figure 6D). No significant differences were observed between the two materials regarding single units and the amplitude of the largest units.

We observed dynamic changes in electrode functions over time (Figure 7). From weeks 0–8, the percentage of electrode sites that were capable of stimulation and recording showed ∼20% fluctuation. A very small fraction of electrodes showed no recording or stimulation capabilities. After week 8, most electrode sites were capable of both stimulation and recording. The total number of electrode sites and distribution of electrode functionality over participating mice are provided in Figure S2.
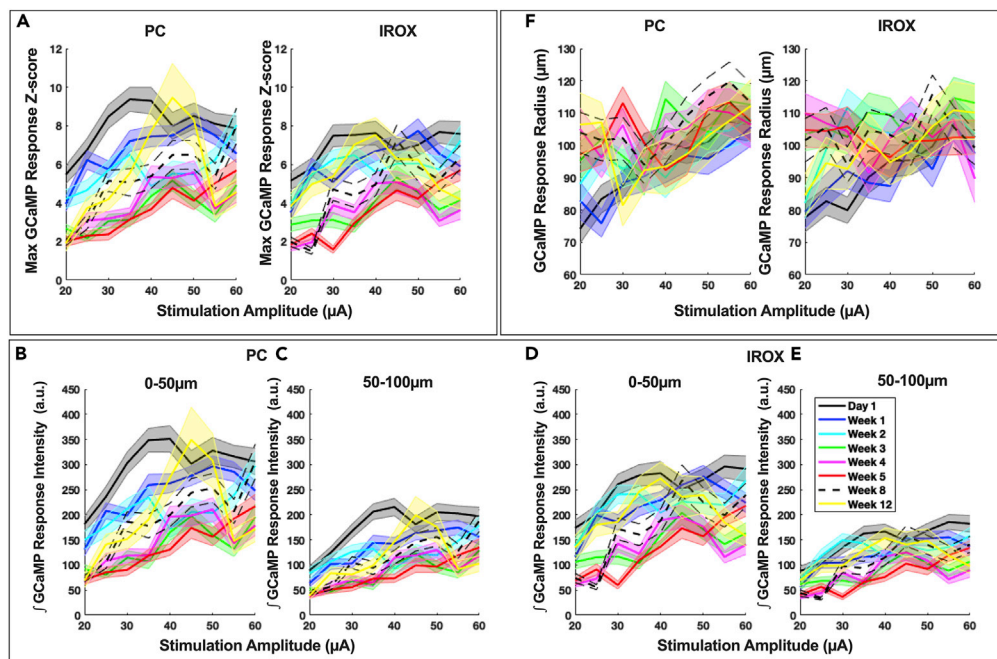
**Figure 3. Quantification of GCaMP response over time**

(A) Maximum GCaMP response *Z* score as a function of stimulation amplitude for PC and IrOx coated electrodes.

(B and C) Integrated GCaMP response as a function of stimulation amplitude by PC coated electrodes for bins 0-50 μm and 50-100 μm, respectively.

(D and E) Integrated GCaMP response as a function of stimulation amplitude by IrOx coated electrodes for bins 0-50 μm and 50-100 μm, respectively.

(F) GCaMP response radius as a function of stimulation amplitude for PC and IrOx coated electrodes. For all images, shaded regions represent the SEM. n = 31–86 electrode sites across 4-11 mice over twelve weeks, for each electrode material. Different colors represent different weeks after implantation and are denoted in (e).

## Longitudinal electrochemical measurements and equivalent circuit modeling

We used electrochemical methods to assess the *in vivo* stability of the electrode materials. Specifically, we measured the electrical impedances of PC and IrOx coated electrodes and quantified the 1 kHz impedance over time (Figure 8A). Among GCaMP response eliciting electrode sites (defined as stimulating electrodes), both materials showed a significant increase in impedance starting at week 3 through week 12, barring fluctuations. While there was no overall significant difference between PC and IrOx impedances, PC coated electrode sites had significantly lower impedance at week 1, and qualitatively lower impedance over the implantation period than IrOx coated electrodes (Figure 8B). For non-stimulating (stimulation that did not elicit a reliable GCaMP response), there was no significant difference between materials (Figure 8C). For stimulating sites, there were significant decreases in cathodic charge storage capacity (CSCc) for both materials as early as week 3 and 5 for PC and IrOx coating, respectively (Figure 8E). For non-stimulating electrodes, there was a reduction in CSCc as early as week 3 for IrOx coated sites (compared to week 1), which showed fluctuations throughout the implantation period. Reduction in non-stimulating PC coated electrode sites occurred as early as week 2 (compared to week 1). Non-stimulating PC-coated electrodes showed significantly lowered CSCc compared to IrOx throughout the implantation period (Figure 8F). Voltage excursions of both electrode material types saw increases in amplitude between day 1 and week 12 (Figure 8G). For stimulating electrodes, PC coated sites showed overall significantly lower energy consumption compared to IrOx coated electrode sites. For both materials, there were significant fluctuations in energy consumption within the first 3 weeks of electrode implant followed by a stable significant increase in energy consumption with minor fluctuation through week 12 (Figure 8H). For non-stimulating electrodes, while there were no significant changes for IrOx, there was a significant increase in energy for PC coated sites at weeks 8 and 10 compared to week 1 (Figure 8I).
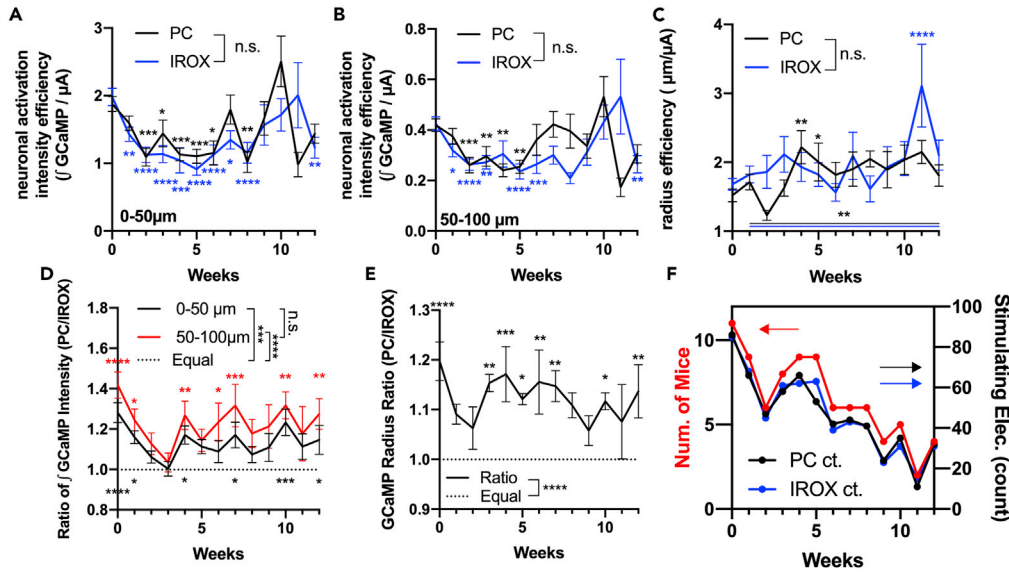
**Figure 4. Quantification of stimulation stability**

(A) Neuronal activation efficiency determined by the integrated GCaMP response per µA for PC and IrOx coated electrodes over time for neuronal elements within 0-50 µm and (B) 50- 100 µm away from the center of the electrode.

(C) Efficiency for the radius of activation determined by µm/µA for PC and IrOx coated electrodes. For (a-c), error bars represent the SEM. Asterisks denote comparisons for each time point to week 0. *p < 0.05, **p < 0.01, ***p < 0.001, ****p < 0.0001.

(D) The ratio of integrated GCaMP intensity (PC sites normalized to its adjacent IrOx sites) over time for neural elements between 0 and 50 µm (black) and 50-100 µm (red). The dashed line represents a reference to equality between the two materials.

(E) The ratio of GCaMP radius (PC sites/IrOx sites) over time. The dashed line represents a reference to equality between the two materials. For (d,e), error bars represent the SEM of the ratios between stimulating PC and IrOx for nine stimulation amplitudes (20- 60 µA). Red and black asterisks denote where ratios are significantly above 1 (equal). *p < 0.05, **p < 0.01, ***p < 0.001, ****p < 0.0001.

(F) The number of mice and the total number of electrode sites analyzed for figures (a–e).

To understand the dynamic changes in the electrode-tissue interface over time, we performed curve fitting of the full spectrum electrochemical impedance spectroscopy to an equivalent circuit model developed by Bisquert et al. (2000) (Figures 9A and 9B) and used by Alba et al. to model electrodes coated with PEDOT/ CNT/Dex (Alba et al., 2015). The model consists of a resistive bulk tissue component (Rser), an encapsulation and electrode coating component (Zd), and the solid portion of the electrode (parallel circuit made of Rct and CPE). Specifically, the Zd circuit consists of a double-channel transmission line distributed element which represents a superposition between a solid and a liquid continuum, or in other words, the tissue encapsulation, and the porous region of the electrode coating, extending from the electrode surface with thickness L. The equation representing Zd is expressed as follows:

$$Zd = \left\{\frac{R_o R_1}{\left[1+\left(\frac{iw}{w1}\right)^\alpha\right]}\right\}^{\frac{1}{2}} \times \coth\left\{\left(\frac{w_1}{w_L}\right)^{\frac{\alpha}{2}}\left[1+\left(\frac{iw}{w1}\right)^\alpha\right]^{\frac{1}{2}}\right\} \qquad \text{(Equation 4-1)}$$

$$w_L = \left(r_0 q_1 L^2\right)^{-\frac{1}{\alpha}} = \left(R_0 Q_1\right)^{-\frac{1}{\alpha}} \qquad \text{(Equation 4-2)}$$

$$w_1 = \left(r_1 q_1\right)^{-\frac{1}{\alpha}} = \left(R_1 Q_1\right)^{-\frac{1}{\alpha}} \qquad \text{(Equation 4-3)}$$

where $r_0$ is the resistance per unit length (ohm cm$^{-1}$) of the electrolyte fluid, $r_1$ is the charge transfer resistance length (ohm cm) of the electrolyte/solid interface, and $q_1$ is the coefficient of the interface CPE per unit length (F s$^{\alpha-1}$ cm$^{-1}$). $\varpi$ is the angular frequency (rad s$^{-1}$) and $i = \sqrt{-1}$. For fitting purposes, L is equated to 1, which results in $R_0$ being the total resistance of the electrolyte phase and represents the restriction to ionic motion within the pores of the coating, and $R_1$ and $Q_1$ represent the total charge transfer resistance and CPE capacitance of the electrolyte/conducting polymer boundary with $\alpha$ representing the
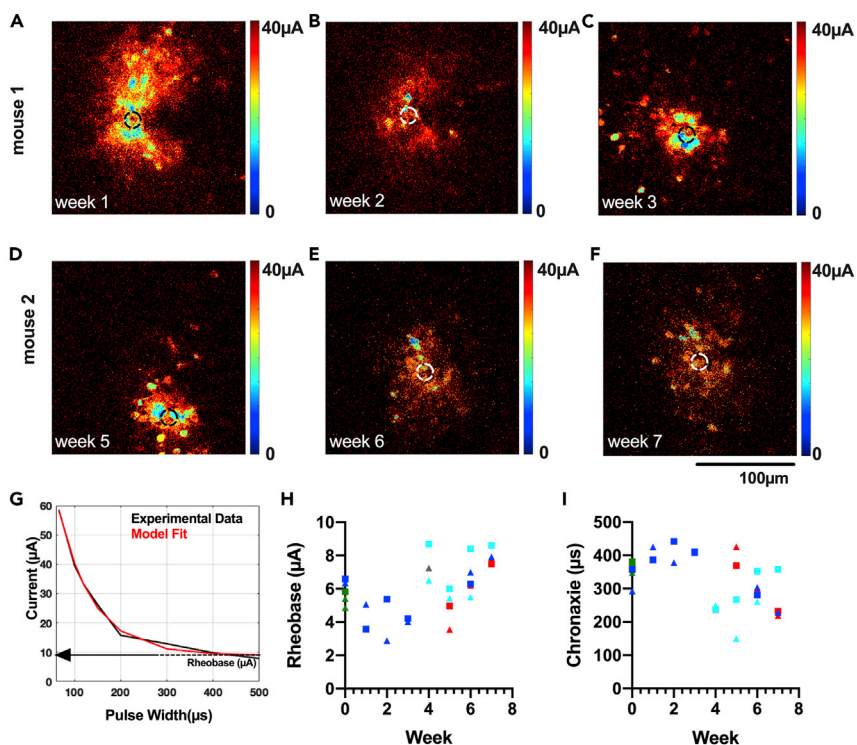
**Figure 5. Two-photon microscopies of neuronal excitability over time**

(A–C) Representative maps of threshold current (100μs pulse width) for neural activation from weeks 1-3 for mouse 1. Black and white dashed circles represent electrode positions.

(D–F) Maps of threshold current for neural activation from weeks 5–7 for mouse 2, from the same electrodeposition as mouse 1. Black and white dashed circles indicate electrode positions. Scale bar represents 100 μm.

(G) Example strength-duration curve from mouse 1. Black trace represents experimental data and red trace represents model fit. Arrows point to rheobase and chronaxie, respectively.

(H) Trends of rheobase and (I) chronaxie of neural elements within 50 μm of the center of the electrodes over time. Symbols represent individual data points from 5 mice where the colors represent different mice. Solid squares represent IrOx sites and solid triangles represent PC sites.

CPE exponential parameter. This equivalent model is a good representation of the electrode-tissue interface for both PC and IrOx as indicated in the representative fitting for day 1 and week 8 after electrode implantation (Figures 9C–9F). This model can accurately depict the resistive behavior at high frequencies of the PC coating and the influence of double-layer capacitance for both materials at lower frequencies over time. Electrolyte resistance ($r_0$) for PC exhibited dynamic changes from week to week within the first two weeks. The increase in electrolyte resistance at week 2 is likely contributed by the accumulation of cells and proteins that could fill the pores of the PC coating. After week 2, electrical stimulation from week to week may result in a variable amount of tissue within the PC film, resulting in variable electrolyte resistance. Meanwhile, the electrolyte resistance for IrOx exhibited no statistically significant change over time. This can be largely attributed to the dramatically smoother surface topography and smaller pore size within the IrOx film compared to the PC coating such that most of the electrolyte resistance is influenced by the tissues encapsulating the electrodes. However, there was an overall significantly lower electrolyte resistance within the PC Zd component compared to IrOx (Figure 9G) due to the higher electrochemical surface area from the nano-fibrous surface topography of PC compared to IrOx sites. This provided ions ample room to diffuse across. PC coated electrodes exhibited overall significantly lower electrolyte resistance compared to IrOx coated electrodes. The capacity coefficient (Q1) of the Zd component for PC coated electrodes showed a significant increase on day 1 compared to the day of surgery. While there was no significant difference between material types, day 1 $Q_1$ of PC coated electrodes was significantly higher than that of IrOx coated electrodes (Figure 9H). The CPE coefficient remained stable with no significant changes over time and between electrode materials (Figure 9J).
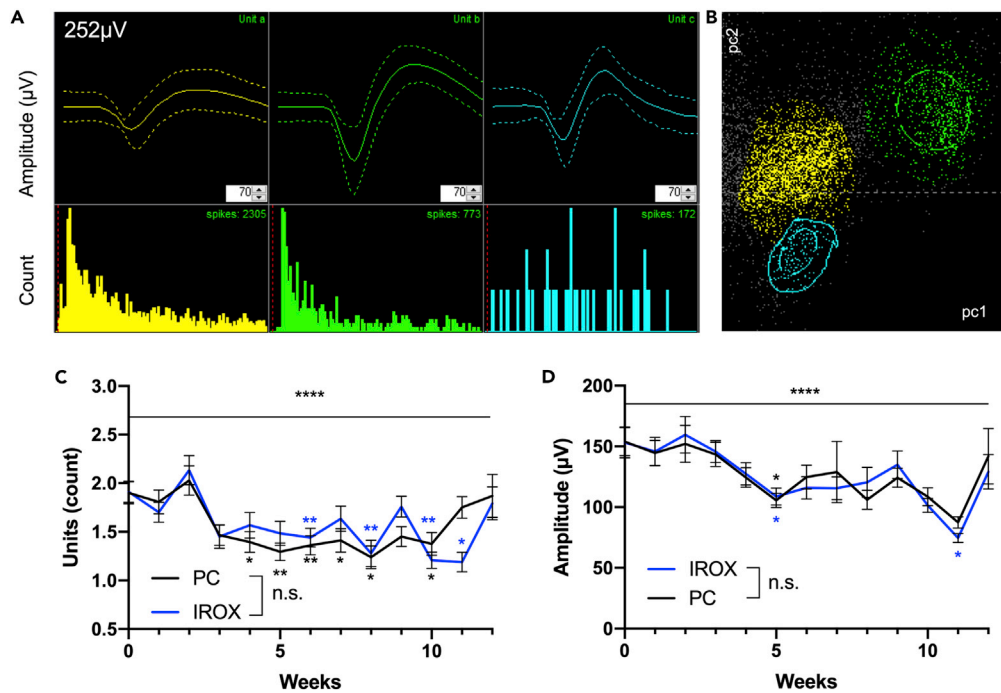
**Figure 6. Electrophysiology over time**

(A) Representative traces of isolated single units from an electrode site with corresponding histograms of inter-spike intervals and (b) the first two principal components for each unit in the PCA space (screen captures from Offline Sorter). 252 μV indicates the amplitude range for the waveform view. (C) Quantification of the number of single units over time. (D) The amplitude of the largest unit for all recording electrode sites. Error bars represent the SEM of electrode sites from a total of 10 mice over time for each electrode material. Electrode sample sizes over time are reported in Figure S1.
*p < 0.05 **p < 0.01, ****p < 0.0001.

### Stimulation induced changes in electrophysiology and impedance

In this study, we observed incidences of the ictal phenomenon, many of which were followed by cortical spreading depression (CSD) during microstimulation. These events manifested in the abnormally high GCaMP response magnitude and response rate to stimulation compared to normal GCaMP response. The current amplitude for the occurrences of ictal phenomena ranged between 40 μA and 60 μA while the current for the occurrences of CSDs ranged between 45 μA and 60 μA. (Figures 10A and 10B). Of these mice that exhibited abnormal neurological events during microstimulation, there was a significant decline in neural recording performances in terms of the number of units per channel (Figure 10C) and amplitude of the largest unit per channel (Figure 10D) for both materials in the 2 min immediately following a stimulation session. Accompanying this was a drastic reduction in the number of electrode sites that were recording neural signals (Figure 10E). The significant reduction in recording performance post-stimulation was likely due to the increased overall metabolic demand from the acute injury in the environment resulting in reduced neuronal activity after electrical stimulation. For both electrode materials, there were significant decreases post-stimulation in the 1 kHz impedance (Figures 10F and 10G). Particularly for PC coated electrodes, there was a significant decrease in the electrolyte resistance across the Zd component after electrical stimulation, but no significant change was detected for IrOx coated electrodes (Figures 10H and 10I).

### Explant investigation

To examine the effects of chronic implantation and electrical stimulation on the electrode arrays. We explanted functional arrays of two mice after 12 weeks of implantation. Both the 4×4 type and the linear array exhibited various levels of material degradation. Using bright field microscopy, we could observe the black appearance characteristic of the PC coatings. However, for the linear array, the black appearance of PC coatings was not apparent for superficial electrode sites (Figures 11A and 11B). The 12-week implantation
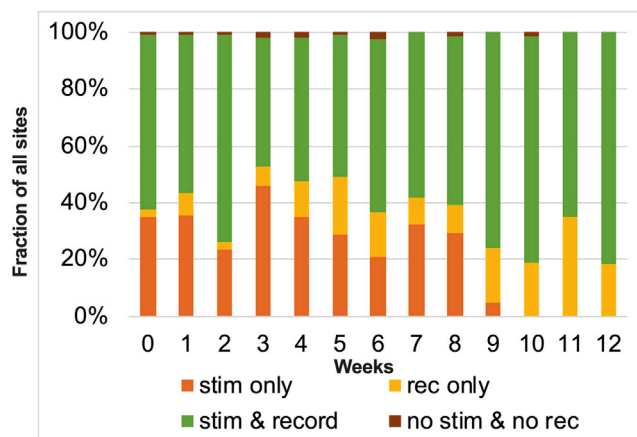
**Figure 7. Functions of electrode sites over time**
Colors represent electrode functions separated by their ability to stimulate GCaMP responses and/or record neural signals. Data combine both electrode materials. The total number of electrode sites and distribution of electrode functionality over participating mice are provided in Figure S2.

and stimulation *in vivo* resulted in a trend of increased electrical impedance for both materials. But due to the variability between electrode sites for each material in the explanted scenario, the increase in impedance was not statistically significant. Additionally, the impedances of PC-coated electrodes were significantly lower than IrOx coatings in both the pre-implant and explanted measurements (Figure 11C). Furthermore, the CSCc for both materials showed a significant decrease in explant compared to pre-implant (Figure 11D). Moreover, there was a significant reduction in charge injection limit for PC coated electrode sites explant compared to pre-implant (Figure 11E). We examined the surface features of the explanted arrays using SEM and observed varying levels of material degradation and tissue adherence for both materials. While some PC sites remained intact over the implant duration, others exhibited features of partial or complete delamination accompanied by tissue encapsulation on the coating material (Figure 11F). Similarly, IrOx sites have exhibited complete or partial delamination or cracking while others remained intact. IrOx degradations were also accompanied by encapsulation that was resistant to our enzymatic treatment (Figure 11G).

## DISCUSSION

The development of modern imaging techniques and transgenic tools enables observations of neural dynamics to electrical stimulations in real-time. In this work, we conducted a longitudinal study on the stability of electrical stimulation performance of two high-charge-injection materials, PC and IrOx. Using NeuroNexus arrays modified with PC and IrOx on alternating sites, we stimulated the somatosensory cortex of GCaMP6s mice for up to twelve weeks using both mesoscale fluorescence imaging and up to seven weeks using two-photon imaging. Meanwhile, we measured electrophysiological and obtained electrochemical signatures of PC and IrOx coated electrodes over time.

### Fluctuations in stimulation efficiency revealed through *in vivo* imaging

We quantified the stability of electrical stimulation using activated GCaMP responses in terms of (1) stimulation efficiencies for each electrode material, i.e., the neuronal activation efficiency and the radius efficiency (Figures 4A–4C), and (2) the ratio of the GCaMP activation magnitude between the two materials (Figures 4D and 4E). We defined two zones for the quantification of neuronal activation efficiency, 0-50 μm and 50-100 μm. In the acute injury phase (weeks 0–2) we observed a significant decline in neuronal activation efficiency in 0-50 μm and 50 -100 μm for both materials. The transient decrease in stimulation efficiency after day one may stem from changes in the neuronal network excitability immediately after the implantation of an electrode which heightened the neuronal response to electrical stimulation on day 1 such that increases in stimulation amplitude resulted in little increases in GCaMP responses. Here, the GCaMP fluorescent signal is an ultrasensitive indicator of action potential events (Chen et al., 2013). Borrowing evidence from mild traumatic brain injury brain slice patch-clamp studies, in acutely injured tissue, both the intact and axotomized neurons exhibited significantly higher action potentials (AP) compared to neurons
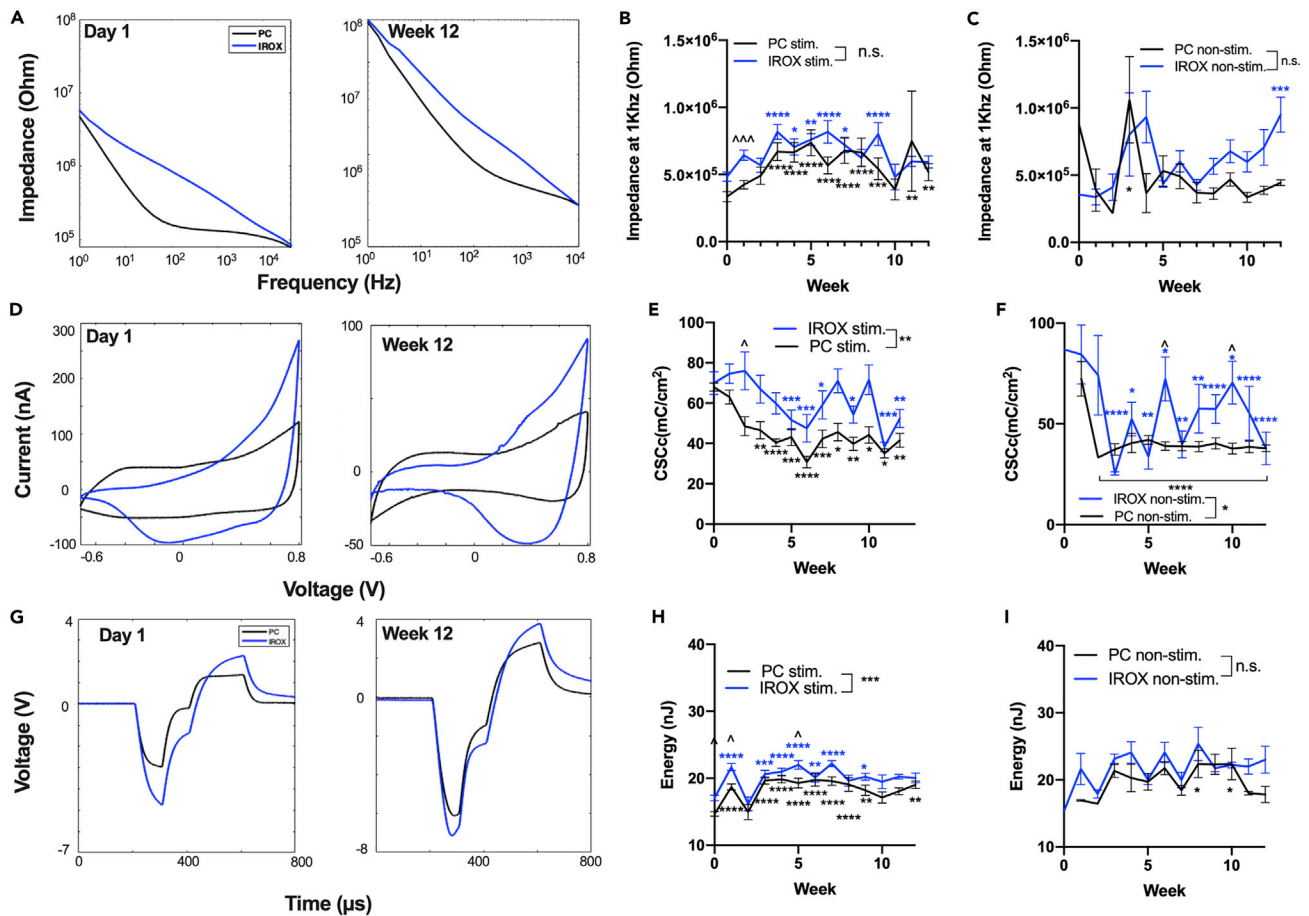
**Figure 8. Electrochemistry measurements over time**

(A) Full-spectrum impedance modulus for electrode sites coated with PC and IrOx for (left) day 1 (right) week 12.

(B) Impedance modulus at 1 kHz for PC and IrOx coated electrodes that elicited GCaMP responses (stim).

(C) Impedance modulus at 1 kHz for PC and IrOx coated electrodes that did not elicit GCaMP responses (non-stim). For (b,c) Carets (^) denote significant difference between material types. Error bars represent the SEM of electrode sites over a total of 11 mice. Electrode sample sizes overtime reported in Figure S3A.

(D) Representative traces of *in vivo* cyclic voltammetry for electrode sites coated with PC and IrOx for day 1(left) and week 12 (right).

(E) Cathodic charge storage capacity for PC and IrOx coated electrodes that elicited GCaMP responses (stim.) (F) Cathodic charge storage capacity for PC and IrOx coated electrodes that did not elicit GCaMP responses (non-stim.). For (E and F) Carets (^) denote significant differences between material types. Error bars represent the SEM of electrode sites from eight mice. Electrode sample sizes over time for both materials are reported in Figure S3B.

(G) Representative traces of voltage excursion from electrodes coated with PC and IrOx on (left) day 1 and (right) week 12.

(H) The energy delivered from stimulating electrodes coated with PC and IrOx over time, Carets (^) denotes significant difference between material types.

(I) Energy delivered from non-stimulating electrodes coated with PC and IrOx over time. For (G and H) error bars represent the SEM of electrode sites from 9 mice. Electrode sample sizes over time for both materials are reported in Figure S3C. In all cases, *p < 0.05, **p < 0.01, ***p < 0.0001, ****p < 0.00001. ^ p < 0.05, ^^^p < 0.0001. Unless otherwise denotes, asterisks in (b,e,h) denote comparisons with week 0. Asterisks in (c,f, i) denote comparisons with week 1, due to the lack of sample size at week 0 for non-stimulating electrodes for statistical comparison. Blue traces represent PC and black traces represent IrOx.

in the un-injured tissues. By 48 hours post-injury, axotomized neurons continued to have high action potential amplitude, whereas the APs in intact neurons recovered compared to neurons in the un-injured tissue. The changes in AP amplitude have been thought to be attributed to various factors such as possible changes in the densities of Na + channels or the K+ ATPase pumps after injury; however, a consensus has not yet been reached regarding the specific mechanism (Katz et al., 2018) (Greer et al., 2012). The severing of network connections due to the acute electrode implantation likely caused axonal injury near the electrode, preventing the efficient recruitment of distant neural elements.

We saw significantly lower neuronal activation efficiency for both materials from week 2 to week 8 for both electrode materials compared to week 0 barring fluctuations for PC at week 7. We saw a gradual recovery in
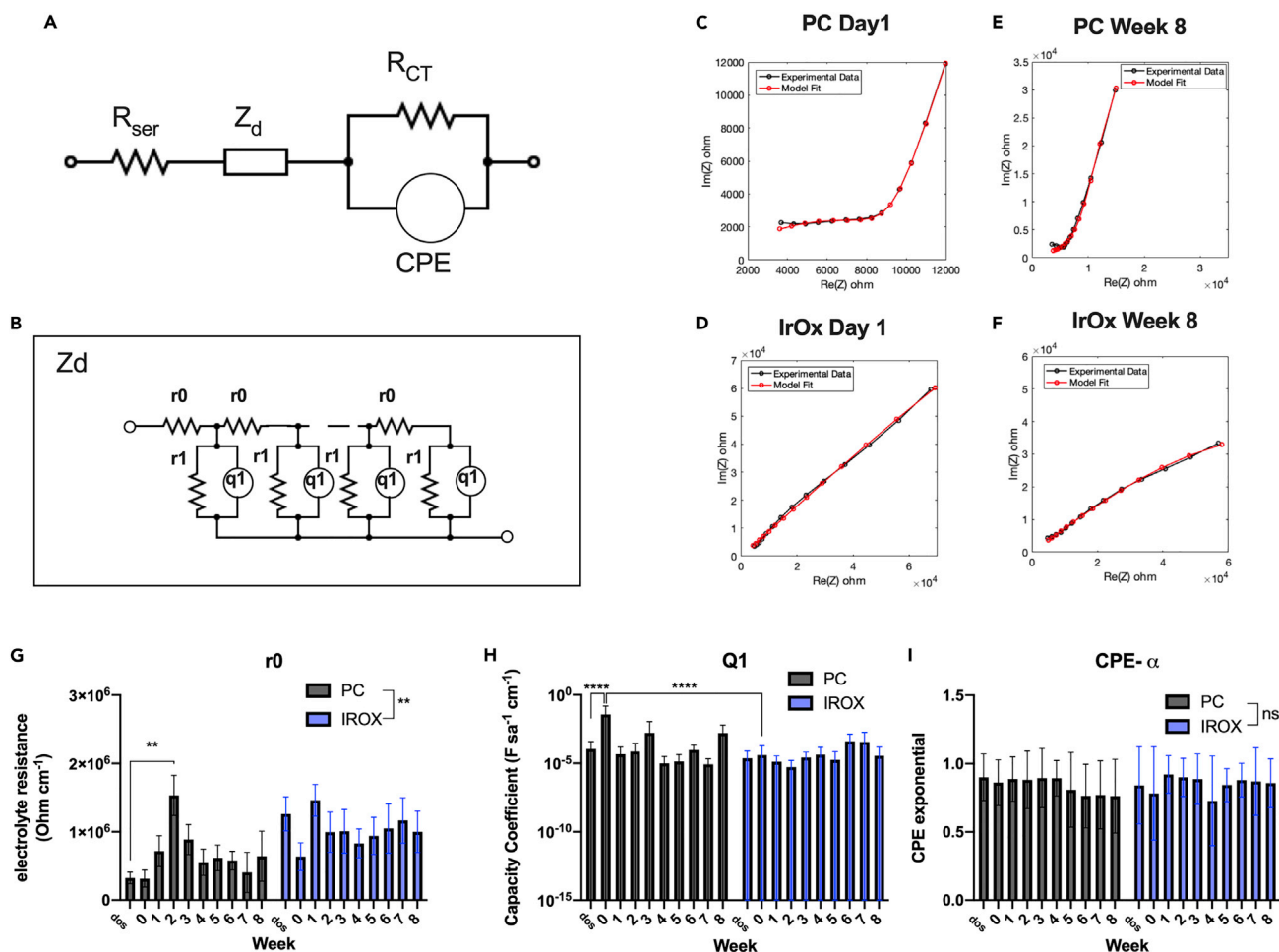
**Figure 9. Equivalent circuit modeling**

(A) Diagram of an equivalent circuit model representing the electrode-tissue interface. Rser represents the resistivity of the bulk tissue. Zd is a diffusion impedance element representing the porous continuum between the tissue encapsulation through the electrode coating. Rct represents the faradaic charge transfer resistance of the solid portion of the electrode, and CPE represents the double-layer capacitance of the solid portion of the electrode.

(B) Details of the Zd circuit, where r0 is the electrolyte resistance (ohm cm$^{-1}$) through the pores of the electrode coating and the encapsulation, and r1 is the charge transfer resistance length (ohm cm). q1 is a CPE representing the electrolyte/conducting polymer boundary. (c,d) Representative fitting for a PC and an IrOx electrode on day 1.

(E and F) Representative fitting for a PC and an IrOx electrode at week 8.

(G) Electrolyte resistance (r0) over time. PC coated electrodes had overall significantly lower electrolyte resistance compared to IrOx coated electrodes. *p < 0.05.

(H) Capacity coefficient Q1 for the q1 CPE element in (B). There was a significant reduction in the capacity coefficient for PC coated electrodes in weeks 1–5 compared to week 0.

(I) CPE exponential, α, of the Zd circuit. (n = 6–32 PC and n = 13–30 IrOx electrode sites from 5 to 9 mice chronically surviving mice).

radius efficiency for both materials over the implant duration, and this may be caused by the initial axonal injury followed by its subsequent regeneration(Figure 4C)

In our previous study (Zheng et al., 2021b), we concluded that PC coated electrodes activate significantly more intense and broader GCaMP responses compared to IrOx coated electrodes acutely. Herein we conducted a longitudinal experiment to investigate if the advantage of the PC coated electrodes in efficient neural stimulation sustains chronically. Same as comparisons made in our previous work, to account for the heterogeneous GCaMP expression and neuronal densities across the cortical depth, we obtained the ratio of the GCaMP response between PC and their IrOx counterparts. We observed significantly higher integrated GCaMP intensity activated by PC coated electrodes compared to IrOx coated electrodes within 50 μm of the at many time points over the implantation period (Figure 4D). However, at weeks 2 - 3, there
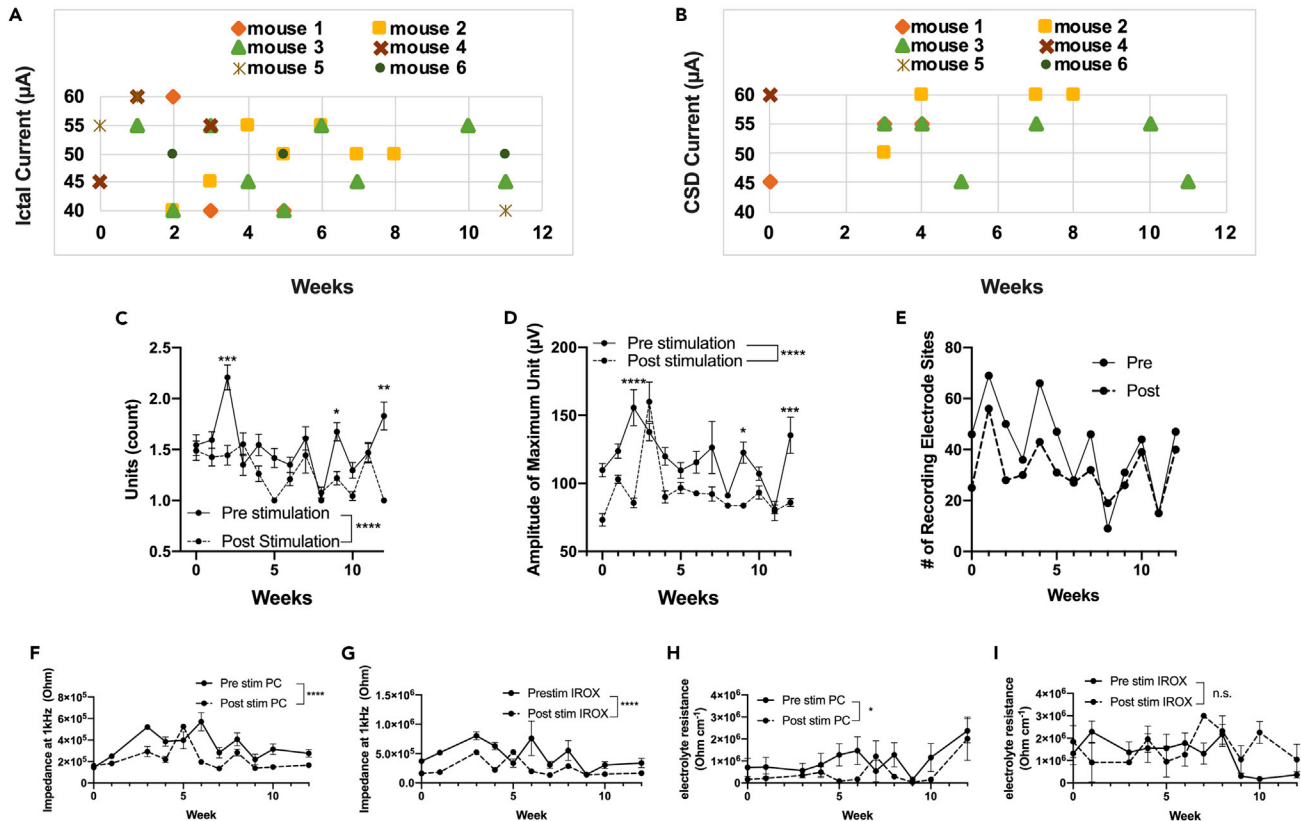
**Figure 10. Observation of abnormal cortical events during microstimulation**

(A) Current for the onset of ictal phenomenon for four mice over 12 weeks.

(B) Current for the onset of cortical spreading depression for four mice over 12 weeks.

(C) The number of single units before and after electrical stimulation for PC and IrOx coated arrays for mice that showed cortical spreading depression (D) Amplitude of largest unit on the array before and after stimulation for mice that showed cortical spreading depression.

(E) The number of electrode sites that were recording neural spikes before and after stimulation over time (N = 5 chronically surviving mice).

(F and G) The impedance at 1 kHz before and after electrical stimulation. n = 8 sites for each electrode material. ****$p < 0.0001$. N = 1 mouse (no CSD).

(H and I) electrolyte resistance across the Zd diffusion layer (r0) for PC and IrOx coated electrodes, respectively. n = 3–7 electrodes that showed adequate model fit over time for PC and n = 4–8 for IrOx. N = 1 mouse (no CSD). Error bars represent the SEM. *$p < 0.05$. See also Video S1.

was no significant difference between electrode materials in the magnitude of the integrated GCaMP responses. This is likely due to (1) the significantly reduced neural elements within 50 μm coupled with (2) the infiltrating inflammatory macrophages and initiation of astrocyte activity in weeks 2 and 3 potentially filling in the pores of the PC coating, which increased the electrolyte resistance of the PC coated electrodes at week 2 (Figure 9G), overriding the benefit the PC coating provides. As the interface recovers with re-established axonal connections along with refreshed PC coating pores after electrical stimulation, the benefit of the PC coating re-emerged. Another potential explanation of PC coatings regaining its higher stimulation efficiency may be supported by evidence in the literature, wherein carbon nanotubes have been demonstrated to support neurite outgrowth (Matsumoto et al., 2010), neuronal health, and reducing inflammation (Kolarcik et al., 2014). We observed non-significant but qualitatively higher integrated GCaMP intensity stimulated by PC coated electrodes in 50-100 μm throughout the implantation period (Figure 4D) compared to the 0-50 μm bin, likely due to (1) higher neural element survival farther away from the implant location (Campbell and Wu, 2018; Azemi et al., 2011), and (2) PC coated electrodes stimulating larger activation radius compared to IrOx coated electrodes. Meanwhile, PC coated electrodes activated a significantly larger radius of neural elements compared to IrOx over the implantation period except for weeks one and two where there were degenerating axons from the insertion of the electrode. As new connections formed, additional neurons were recruited, and the benefit of the PC coating re-emerged (Figures 4C and 4E). Using TPM, we examined the excitability of five mice with the same preparation. We quantified excitability in terms of the rheobase of neural elements within 50 μm of the electrode.
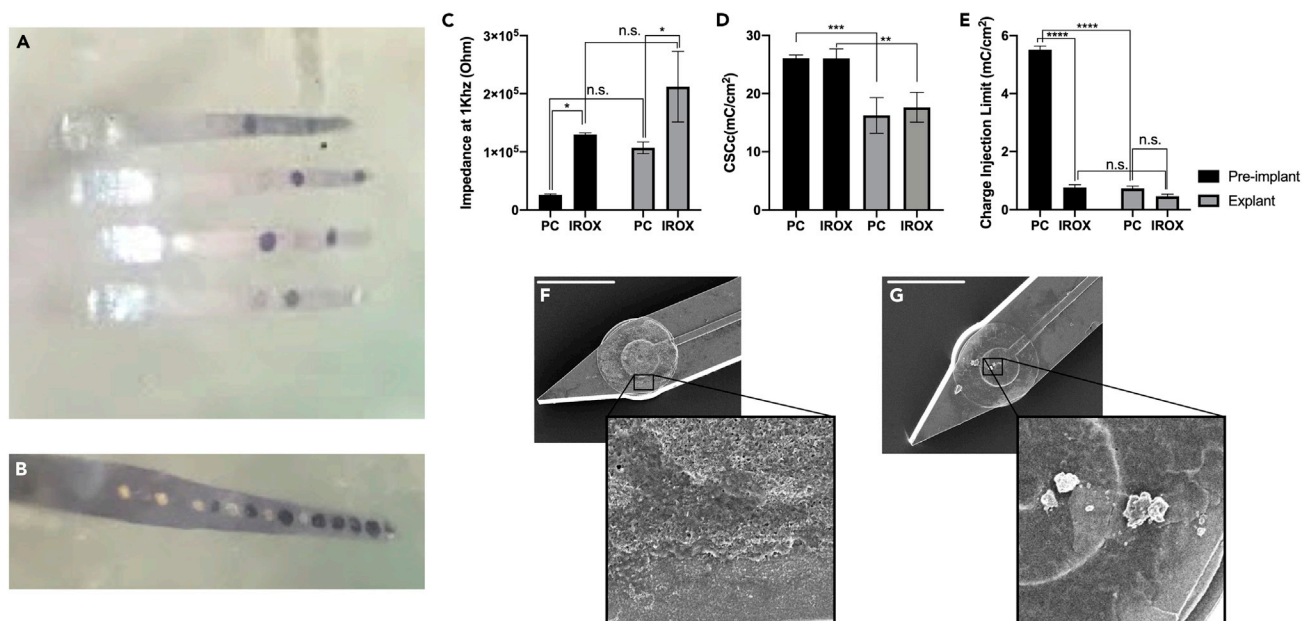
**Figure 11. Explant analysis**

(A and B) optical micrographs of four-shank and single shank arrays coated with PC and IrOx.

(C) The impedance at 1 kHz of electrodes coated with PC and IrOx as pre implants and explants. *p < 0.05.

(D) Cathodic charge storage capacity of electrodes coated with PC and IrOx as pre-implants and explants. **p < 0.01, ***p < 0.001.

(E) Charge injection limit of electrodes coated with PC and IrOx as pre-implants and explants. ****p < 0.00001. Error bars are SEM of n = 16 PC coated and n = 13 IrOx coated functional sites over two electrode arrays.

(F) SEM of an explanted PC electrode. Inset shows a magnified view of the explanted surface. Note evidence of coating delamination and tissue adherence on the surface of the electrode site.

(G) SEM of an explanted IrOx electrode. Inset shows a magnified view of the explanted surface. Note evidence of cracking in the IrOx thin film and tissue coverage on the surface of the electrode.

There was a qualitative increase in rheobase and a decrease in chronaxie from week one to week 7, suggesting a decrease in excitability for neural elements in this region. Supporting this observation, the Purcell group has performed *ex vivo* studies on quantifying the expressions of ion channels involved in neuronal signal transduction, they have found a progressive increase in potassium channel expression and a reduction in sodium channel expression that accompanied a 6-week signal loss in terms of local field potentials and the number of single units, changes in these ion channel expressions have been shown to reduce the excitability of neurons (Salatino et al., 2019). Accordingly, we have also observed a decline in neuronal signals within this period (Figure 6).

### Longitudinal changes in electrophysiological measurements

Recordings of spontaneous spike activity showed an overall significant decline in single-unit counts and the amplitude of the largest unit for both materials. However, there was no significant decline in neural recording performance for either material within 2 weeks after implantation as observed in the stimulation efficiency investigation. This observation may be explained by the differing mechanisms in neural recording and stimulation. In neural recording, the signals were more likely to be coming from the cell soma, whereas stimulation is initiated at the axons. As previously characterized in our laboratory, the implantation of an electrode into the neural tissue asserts mechanical strains on the neuronal somas, which increases the intracellular calcium levels, but more aggressively severs the axons and neurites perpendicular to the path of the electrode insertion. This results in acute neurite "blebbing," which are swollen, hypertrophic spherical bodies that develop along neurites following trauma (Eles et al., 2018). Sustained high levels of intracellular calcium and axonal blebbing have been reported to promote neural degeneration and the loss of synaptic connectivity. The loss of synaptic connectivity prevents the additional recruitment of distant neurons with electrical stimulation but may not change the spontaneous activity of intact neurons nearby the electrode. We observed a more gradual decline in neural recording performance in both electrode materials, and we

attribute this observation to (1) the gradual buildup of the glial scar around the electrode sites, and (2) the continuous neural degeneration near the electrode due to persistent blood barrier disruption triggering additional inflammations that lead to neuronal death because of micro-motion, respiration, and animal movements. It is worth noting the potential differences between a passive interface (recording only) and an active interface (stimulating and recording). It is acknowledged that electrophysiological data from passively recording electrodes decline over the first three months (Kozai et al., 2015b). Where scarring may have the potential to build over time reducing recording quality in terms of the number of units as well as unit amplitudes. On the other hand, a stimulating electrode-tissue interface may become less predictable due to potential changes in the interface induced by passing electrical currents which have the potential to create openings in the glial scar, resulting in decreased electrical impedance and electrolyte resistance (Figures 10F–10H).

We surveyed electrode functions in their abilities to stimulate and record neural activity and found fluctuations in electrode functions over time. While a large fraction of electrode sites was capable of both stimulation and recording, a small fraction of electrodes could only stimulate or record neural activity. Electrodes that were only stimulating may be distant from a neuronal soma but close enough to an axon hillock for initiation of action potential. Electrodes that are only recorded may have undergone material degradation that prohibits the injection of sufficient charge to reach the threshold of neural activation. Electrode sites that failed to stimulate and record neural activities are likely sites that were superficial or sites whose traces disconnected due to failure under mechanical strain *in vivo* (Kozai et al., 2015a).

## PC is a more energy-efficient material for chronic stimulation

We performed comprehensive *in vivo* electrochemical measurements of both electrode materials chronically and observed distinct differences in the electrochemical features of electrodes that activated GCaMP responses versus electrodes that did not. Specifically, stimulating PC electrodes showed significantly lower impedance at 1 kHz in the acute phase and significantly lower delivered energy throughout the implantation period compared to IrOx electrodes. On the other hand, there were no significant differences in impedance and delivered energy between the two electrode materials for non-stimulating electrode sites. For both stimulating and non-stimulating electrodes, the CSCc, in general, is slightly higher in IrOx than PC, which is consistent with their starting values measured *in vitro*. Specifically, when normalized by the geometric surface area the CSCc for PC and IrOx sites were 21.12 ± 0.3 and 25.1 ± 1.9, respectively (Zheng et al., 2021b). For the same stimulating material, we observed that non-stimulating PC electrodes tend to exhibit lowered CSCc and relatively higher delivered energy compared to stimulating PC electrodes. The lowered CSCc and increased delivered energy were likely due to potential changes in the PC coating, especially in some superficial sites. The superficial electrode sites not only need to endure the mechanical stress imposed by brain micro-motion and drastic animal movements but there are also additional shear forces on the electrode material as the electrode fluctuates in and out of the brain parenchyma, likely overcoming the adhesion force of the PC coating with the iridium substrate, resulting in a faster electrode material degradation. Explant investigations showed that many PC coating delaminations, indeed, occurred on superficial sites in the linear array. No location-specific material degradation was observed in multi-shank arrays as all sites are well below the brain boundary. The degree of material degradation is less in IrOx coated superficial sites possibility due to its smoother surface topography which reduces its friction with the brain tissue, preventing catastrophic delamination.

Nevertheless, comprehensive electrochemical measurements of both electrode materials suggest that PC is a better candidate for higher energy-efficient stimulation compared to IrOx. This is supported by (1) the significantly lower electrical impedances at 1 kHz for stimulating electrodes over the acute phase of the implant compared to IrOx (Figure 8B) and (2) significantly lowered electrode potential (energy) from PC coated stimulating electrodes over the 12 weeks (Figure 8J). These features will reduce the power consumption in chronically implanted pulse generators, reducing the frequency of battery replacement surgeries.

## Abnormal cortical events to electrical microstimulation

In this study, we observed numerous ictal phenomena during microstimulation. These events manifested in the abnormally high GCaMP response magnitude and response rate to stimulation compared to

normal GCaMP responses. Some cases of the ictal phenomenon were followed by cortical spreading depressions marked by sweeping calcium events across the cortical surface and silencing of the cortex, lasting up to a minute, with the gradual but eventual recovery of spontaneous calcium activity (Video S1, Ictal phenomenon, related to Figure 10). While we have no definitive answer to the exact mechanism for which these incidences occurred, there are several potential explanations. In seizure research, electrical kindling is used as a tool to reliably initiate seizure activity in animal models which was first proposed by Goddard et al. (Goddard, 1967). The kindling is induced by repeated stimulation that evokes afterdischarges (AD), which are high amplitude, rhythmic activities observed in the electrocorticogram (EEG), outlasting the stimulus train (Grabenstatter and Sutula, 2009), these EEG activities can be inferred with GCaMP signals in our study. The parameters for electric kindling typically consist of trains of pulses 1-2 s in duration, 1 ms in pulse width, and 25–150 Hz in frequency (Yoo et al., 2017). The current threshold for kindling is determined by increasing stimulation amplitude in small increments until AD occurs, which can vary between animals and animal models (Jalilifar et al., 2017). While the mechanical trauma introduced by the insertion of an electrode could contribute to the onset of CSDs, as revealed in our previous investigation (Eles et al., 2018). It is unlikely that the chronic presence of the electrode promoted the occurrence of CSDs in our study because they were only linked to electrical stimulations above 40 µA (or 4 nC/ph Figures 10A and 10B). Also supporting this claim, Cela et al. reliably triggered epilepsy in layers II/III using optogenetics (Cela et al., 2019). The occurrence of CSDs could be due to repeated neuronal depolarizations which could increase the extracellular glutamate and potassium concentrations to cytotoxic levels, increasing the likelihood of epilepsy (Cho, 2013). In our study, the neuronal suppression after CSDs were reversible; while the number of units and the amplitude of the units significantly declined after electrical stimulation, these metrics showed improvement before electrical stimulation the following week (Figure 10C and 10D). While these kindling events only occurred in a subset of our subjects, the delivered charge per phase, duty cycle, and stimulation frequency is in the range of values used in other animal models and human studies, calling for further studies to investigate if they cause any permanent neural damage and ways to avoid them (Flesher et al., 2016; Kim et al., 2017; Deprez et al., 2018; Huang et al., 2019; Yadav et al., 2020).

In summary, modern imaging techniques and transgenic tools enable observations of neural dynamics to electrical stimulations in real-time. Herein, we chronically stimulated the cortex of GCaMP6s mice using two high-charge-injection materials, PC and IrOx, for up to 12 weeks. We observed dynamic changes in stimulation efficiency in terms of integrated GCaMP intensity and radius per unit stimulation amplitude. Using TPM, we evaluated the excitability of neural elements within 50 µm of the electrode and observed a qualitative increase in the rheobase over 7 weeks, indicating qualitative decreased excitability within the first 50 µm of the electrode center. Spontaneous electrophysiology showed a significant decline in neural spike unit count and amplitude over time for both materials. Electrochemical measurements suggest that PC coated electrodes are more energy-efficient at stimulating GCaMP responses compared to IrOx coated electrodes, chronically. Furthermore, we observed abnormal cortical responses to stimulations within the charge injection limit of both electrode materials in a subset of chronically surviving mice, providing new evidence for the potential adverse effects of widely used intracortical stimulation paradigms. Results from this study not only revealed the dynamic changes in stimulation efficiency after implantation but also reiterates the tremendous potential for PC to be used for high-efficiency chronic stimulations in neuromodulation.

### Limitations of the study

Due to complications associated with chronic cranial window prep in mice, it is challenging to image consistently from the same electrode sites using TPM. Therefore, the data presented in Figure 5 are a qualitative analysis of a cumulative view of mice from which we were able to observe the electrode-tissue interface. The cranial window clarity could be better improved using special sealants (Kozai et al., 2016b) and micro prisms (Yang et al., 2021). As observed in Figures 4F and Table S1 stimulation was skipped in some cases due to a few mice needing additional recovery after the surgery or instrumentation-related issues. However, our stimulation paradigm is mild compared to what is conducted clinically and should not have significant effects that last until the next week. In our study, we used GCaMP activation area via PC and IrOx to demonstrate the different efficiencies between the materials. An alternative explanation to the observed efficiency differences could be due to the formation of new connections in cortical neural circuits due to different levels of neuroplasticity in the presence of different electrode coatings. A potential approach to investigate the potential strengthening in neuronal connections upon repeated

stimulation may employ the use of *in vitro* cell culture. Wherein, primary neurons may be cultured on the surface of electrodes of different coatings where electrical stimulation is delivered periodically. To assess the strengthening or weakening of synaptic connections, one might compare the postsynaptic potential to the same presynaptic input over time with and without electrical stimulation. Moreover, as revealed by explant analyses, there were cases of electrode material failure such as cracking and delamination. Before implantation, *in vitro* characterizations of the charge injection limit of both electrode materials indicated that our maximum current amplitude 6 nC/ph was below the −0.6V hydrolysis window for both electrode materials. Material degradation will inherently reduce the effective surface area for stimulation and reduce the charge injection limit. However, using our stimulation paradigm, we did not observe overt signs of gas evolution as observed in using electrode rejuvenation protocols (monopolar 4s + 1.5V (Eles et al., 2018)). Improvement in the adhesion of the coating material with its underlying substrate will likely result in a more stable stimulation efficiency for both materials (Zheng et al., 2021a). Additionally, the stimulation intensity, frequency, and duty cycle in this study were applied weekly, which is mild compared to some clinical application conditions where electrical stimulations may be required 24 h a day. To determine if PC shows continuous stimulation benefit compared to IrOx coated electrodes, more aggressive *in vivo* stimulation experiments should be performed. While we have demonstrated PC to be more efficient the results of this study do not provide a clear answer for if and how the increased efficiency translates to changes in neural functions and rehabilitation. Additional investigations of electrical stimulation efficiency should pair *in vivo* imaging with behavior for a comprehensive evaluation. Furthermore, the authors acknowledge potential limitations to the semi-manual spike sorting used here. However, the sorting method here (k-means clustering followed by the inspection of sorting result) was used consistently across all analyses from the same researcher without prior knowledge of electrode mapping and hence coating type. In future studies, we will employ a fully automated sorting method that utilizes a battery of spike quality metrics including L-ratio (Buccino et al., 2020). Finally, our study was limited to observing the activities of neural elements only with no additional histological analysis (due to complications with extracting the probes). To further understand the stimulating interface, additional cellular and molecular analysis may be used to understand the behavior of non-neuronal cells such as microglia, astrocytes, oligodendrocytes, and pericytes, in conjunction with neural element labels.

## STAR★METHODS

Detailed methods are provided in the online version of this paper and include the following:

- KEY RESOURCES TABLE
- RESOURCE AVAILABILITY
  - ○ Lead contact
  - ○ Materials availability
  - ○ Data and code availability
- EXPERIMENTAL MODEL AND SUBJECT DETAILS
  - ○ Electrode modification
  - ○ Animal surgery
  - ○ *In vivo* imaging and electrical stimulation
  - ○ Image analysis
  - ○ Electrophysiology
  - ○ Electrochemistry and equivalent circuit modeling
  - ○ Explant analysis
- QUANTIFICATION AND STATISTICAL ANALYSES

## SUPPLEMENTAL INFORMATION

Supplemental information can be found online at https://doi.org/10.1016/j.isci.2022.104539.

## AUTHOR CONTRIBUTIONS

X.S.Z., X.T.C. Conceived and designed the study, X.S.Z. and Q.Y. performed animal surgery, A.V., X.S.Z., and X.T.C. designed the analysis, X.S.Z. performed data collection and data analysis. X.S.Z. wrote the article, Q.Y., A.V., and X.T.C. edited the article.

## DECLARATION OF INTERESTS

The authors report no conflict of interest.

## REFERENCES

Global Neuromodulation Market Size Study, By Technology (Internal Neuromodulation, External Neuromodulation), by Application (Parkinson's Disease, Epilepsy, Depression, Dystonia, Pain Management, Others) and Regional Forecasts 2020-2027.

Alba, N.A., Du, Z.J., Catt, K.A., Kozai, T.D.Y., and Cui, X.T. (2015). In vivo electrochemical analysis of a PEDOT/MWCNT neural electrode coating. Biosensors 5, 618–646. https://doi.org/10.3390/bios5040618.

Allahyari, Z., Haghighipour, N., Moztarzadeh, F., Ghazizadeh, L., Hamrang, M., Shokrgozar, M.A., and Gholizadeh, S. (2016). Optimization of electrical stimulation parameters for MG-63 cell proliferation on chitosan/functionalized multiwalled carbon nanotube films. RSC Adv. 6, 109902–109915. https://doi.org/10.1039/c6ra24407f.

Azemi, E., Lagenaur, C.F., and Cui, X.T. (2011). The surface immobilization of the neural adhesion molecule L1 on neural probes and its effect on neuronal density and gliosis at the probe/tissue interface. Biomaterials 32, 681–692. https://doi.org/10.1016/j.biomaterials.2010.09.033.

Bent, B., Chiang, C., Wang, C., Lad, N., Kent, A., and Viventi, J. (2019). Simultaneous recording and stimulation instrumentation for closed loop spinal cord stimulation. In 9th International IEEE/EMBS Conference on Neural Engineering (NER), 20-23 March 2019 2019, pp. 694–697.

Bisquert, J., Belmonte, G.G., Santiago, F.F., Ferriols, N.S., Yamashita, M., and Pereira, E.C. (2000). Application of a distributed impedance model in the analysis of conducting polymer films. Electrochem. Commun. 2, 601–605. https://doi.org/10.1016/s1388-2481(00)00089-8.

Buccino, A.P., Hurwitz, C.L., Garcia, S., Magland, J., Siegle, J.H., Hurwitz, R., and Hennig, M.H. (2020). SpikeInterface, a unified framework for spike sorting. Elife 9, e61834. https://doi.org/10.7554/elife.61834.

Buettner, G.R. (1993). The pecking order of free radicals and antioxidants: lipid peroxidation, -tocopherol, and ascorbate. Arch. Biochem. Biophys. 300, 535–543. https://doi.org/10.1006/abbi.1993.1074.

Bullard, A.J., Hutchison, B.C., Lee, J., Chestek, C.A., and Patil, P.G. (2020). Estimating risk for future intracranial, fully implanted, modular neuroprosthetic systems: a systematic review of hardware complications in clinical deep brain stimulation and experimental human intracortical arrays. Neuromodulation 23, 411–426. https://doi.org/10.1111/ner.13069.

Caldwell, R., Street, M.G., Sharma, R., Takmakov, P., Baker, B., and Rieth, L. (2020). Characterization of Parylene-C degradation mechanisms: in vitro reactive accelerated aging model compared to multiyear in vivo implantation. Biomaterials 232, 119731. https://doi.org/10.1016/j.biomaterials.2019.119731.

Campbell, A., and Wu, C. (2018). Chronically implanted intracranial electrodes: tissue reaction and electrical changes. Micromachines 9, 430. https://doi.org/10.3390/mi9090430.

Cela, E., Mcfarlan, A.R., Chung, A.J., Wang, T., Chierzi, S., Murai, K.K., and Sjöström, P.J. (2019). An optogenetic kindling model of neocortical epilepsy. Sci. Rep. 9, 5236. https://doi.org/10.1038/s41598-019-41533-2.

Chan, P.H., Yurko, M., and Fishman, R.A. (1982). Phospholipid degradation and cellular edema induced by free radicals in brain cortical slices. J. Neurochem. 38, 525–531. https://doi.org/10.1111/j.1471-4159.1982.tb08659.x.

Chen, K., Wellman, S.M., Yaxiaer, Y., Eles, J.R., and Kozai, T.D.Y. (2021). In vivo spatiotemporal patterns of oligodendrocyte and myelin damage at the neural electrode interface. Biomaterials, 120526. https://doi.org/10.1016/j.biomaterials.2020.120526.

Chen, T.-W., Wardill, T.J., Sun, Y., Pulver, S.R., Renninger, S.L., Baohan, A., Schreiter, E.R., Kerr, R.A., Orger, M.B., Jayaraman, V., et al. (2013). Ultrasensitive fluorescent proteins for imaging neuronal activity. Nature 499, 295–300. https://doi.org/10.1038/nature12354.

Chia, L., Thompson, J., and Moscarello, M. (1983). Disorder in human myelin induced by superoxide radical: an investigation. Biochem. Biophys. Res. Commun. 117, 141–146. https://doi.org/10.1016/0006-291x(83)91552-8.

Cho, C.H. (2013). New mechanism for glutamate hypothesis in epilepsy. Front. Cell. Neurosci. 7, 127. https://doi.org/10.3389/fncel.2013.00127.

Cogan, S.F., Plante, T., and Ehrlich, J. (2004). Sputtered iridium oxide films (SIROFs) for low-impedance neural stimulation and recording electrodes. In The 26th Annual International Conference of the IEEE Engineering in Medicine and Biology Society (IEEE), pp. 4153–4156.

Cui, X.T., and Zhou, D.D. (2007). Poly (3, 4-ethylenedioxythiophene) for chronic neural stimulation. IEEE. Trans. Neural. Syst. Rehabil. Eng. 15, 502–508. https://doi.org/10.1109/tnsre.2007.909811.

Dana, H., Chen, T.-W., Hu, A., Shields, B.C., Guo, C., Looger, L.L., Kim, D.S., and Svoboda, K. (2014). Thy1-GCaMP6 transgenic mice for neuronal population imaging in vivo. PLoS One 9, e108697. https://doi.org/10.1371/journal.pone.0108697.

Daniels, D.H., Powell, C.R., Braasch, M.R., and Kreder, K.J. (2010). Sacral neuromodulation in diabetic patients: success and complications in the treatment of voiding dysfunction. Neurourol. Urodyn 29, 578–581. https://doi.org/10.1002/nau.20791.

Deprez, M., Luyck, K., Luyten, L., Tambuyzer, T., Nuttin, B., and Mc Laughlin, M. (2018). An evaluation of the effect of pulse-shape on grey and white matter stimulation in the rat brain. Sci. Rep. 8, 752. https://doi.org/10.1038/s41598-017-19023-0.

Duan, Y., Clark, G.M., and Cowan, R. (2004). A study of intra-cochlear electrodes and tissue interface by electrochemical impedance methods in vivo. Biomaterials 25, 3813–3828. https://doi.org/10.1016/j.biomaterials.2003.09.107.

Eles, J.R., and Kozai, T.D. (2020). In vivo imaging of calcium and glutamate responses to intracortical microstimulation reveals distinct temporal responses of the neuropil and somatic compartments in layer II/III neurons. Biomaterials 234, 119767. https://doi.org/10.1016/j.biomaterials.2020.119767.

Eles, J.R., Vazquez, A.L., Kozai, T.D.Y., and Cui, X.T. (2018). In vivo imaging of neuronal calcium during electrode implantation: spatial and temporal mapping of damage and recovery. Biomaterials 174, 79–94. https://doi.org/10.1016/j.biomaterials.2018.04.043.

Eles, J.R., Vazquez, A.L., Snyder, N.R., Lagenaur, C., Murphy, M.C., Kozai, T.D.Y., and Cui, X.T. (2017). Neuroadhesive L1 coating attenuates acute microglial attachment to neural electrodes as revealed by live two-photon microscopy. Biomaterials 113, 279–292. https://doi.org/10.1016/j.biomaterials.2016.10.054.

Flesher, S.N., Collinger, J.L., Foldes, S.T., Weiss, J.M., Downey, J.E., Tyler-Kabara, E.C., Bensmaia, S.J., Schwartz, A.B., Boninger, M.L., and Gaunt, R.A. (2016). Intracortical microstimulation of human somatosensory cortex. Sci. Transl. Med. 8, 361ra141. https://doi.org/10.1126/scitranslmed.aaf8083.

Goddard, G.V. (1967). Development of epileptic seizures through brain stimulation at low intensity. Nature 214, 1020–1021. https://doi.org/10.1038/2141020a0.

Grabenstatter, H.L., and Sutula, T.P. (2009). MODELS | kindling: a phenomenon of seizure-induced plasticity and a model of focal and limbic epilepsy. In Encyclopedia of Basic Epilepsy Research, P.A. Schwartzkroin, ed. (Oxford: Academic Press).

Greer, J.E., Povlishock, J.T., and Jacobs, K.M. (2012). Electrophysiological abnormalities in both axotomized and nonaxotomized pyramidal neurons following mild traumatic brain injury. J. Neurosci. 32, 6682–6687. https://doi.org/10.1523/jneurosci.0881-12.2012.

Griot, C., Vandevelde, M., Richard, A., and Peterhans, E. (1990). Selective degeneration of oligodendrocytes mediated by reactive oxygen species. Free. Radic. Res. Commun. 11, 181–193. https://doi.org/10.3109/10715769009088915.

Guo, J., Jin, H., Shi, Z., Yin, J., Pasricha, T., and Chen, J.D.Z. (2019). Sacral nerve stimulation improves colonic inflammation mediated by autonomic-inflammatory cytokine mechanism in rats. Neuro Gastroenterol. Motil. 31, e13676. https://doi.org/10.1111/nmo.13676.

Hambrecht, F.T. (1995). Visual prostheses based on direct interfaces with the visual system. Bailliere. Clin. Neurol. 4, 147–165.

Huang, Y., Hajnal, B., Entz, L., Fabó, D., Herrero, J.L., Mehta, A.D., and Keller, C.J. (2019). Intracortical dynamics underlying repetitive stimulation predicts changes in network connectivity. J. Neurosci. 39, 6122–6135. https://doi.org/10.1523/jneurosci.0535-19.2019.

Jalilifar, M., Yadollahpour, A., Moazedi, A.A., and Ghotbeddin, Z. (2017). Low frequency electrical stimulation either prior to or after rapid kindling stimulation inhibits the kindling-induced epileptogenesis. BioMed Res. Int. 2017, 1–8. https://doi.org/10.1155/2017/8623743.

Katz, E., Stoler, O., Scheller, A., Khrapunsky, Y., Goebbels, S., Kirchhoff, F., Gutnick, M.J., Wolf, F., and Fleidervish, I.A. (2018). Role of sodium channel subtype in action potential generation by neocortical pyramidal neurons. Proc. Natl. Acad. Sci. USA 115, E7184–E7192. https://doi.org/10.1073/pnas.1720493115.

Kim, S., Callier, T., and Bensmaia, S.J. (2017). A computational model that predicts behavioral sensitivity to intracortical microstimulation.

J. Neural. Eng. 14, 016012. https://doi.org/10.1088/1741-2552/14/1/016012.

King, K.W., Cusack, W.F., Nanivadekar, A.C., Ayers, C.A., Urbin, M.A., Gaunt, R.A., Fisher, L.E., and Weber, D.J. (2019). DRG microstimulation evokes postural responses in awake, standing felines. J. Neural. Eng. 17, 016014. https://doi.org/10.1088/1741-2552/ab50f4.

Kolarcik, C.L., Catt, K., Rost, E., Albrecht, I.N., Bourbeau, D., Du, Z., Kozai, T.D.Y., Luo, X., Weber, D.J., and Tracy Cui, X. (2014). Evaluation of poly(3, 4-ethylenedioxythiophene)/carbon nanotube neural electrode coatings for stimulation in the dorsal root ganglion. J. Neural. Eng. 12, 016008. https://doi.org/10.1088/1741-2560/12/1/016008.

Konat, G.W., and Wiggins, R.C. (1985). Effect of reactive oxygen species on myelin membrane proteins. J. Neurochem. 45, 1113–1118. https://doi.org/10.1111/j.1471-4159.1985.tb05530.x.

Kozai, T.D., Catt, K., Li, X., Gugel, Z.V., Olafsson, V.T., Vazquez, A.L., and Cui, X.T. (2015a). Mechanical failure modes of chronically implanted planar silicon-based neural probes for laminar recording. Biomaterials 37, 25–39. https://doi.org/10.1016/j.biomaterials.2014.10.040.

Kozai, T.D., Jaquins-Gerstl, A.S., Vazquez, A.L., Michael, A.C., and Cui, X.T. (2016a). Dexamethasone retrodialysis attenuates microglial response to implanted probes in vivo. Biomaterials 87, 157–169. https://doi.org/10.1016/j.biomaterials.2016.02.013.

Kozai, T.D.Y., Eles, J.R., Vazquez, A.L., and Cui, X.T. (2016b). Two-photon imaging of chronically implanted neural electrodes: sealing methods and new insights. J. Neurosci. Methods. 258, 46–55. https://doi.org/10.1016/j.jneumeth.2015.10.007.

Kozai, T.D.Y., Jaquins-Gerstl, A.S., Vazquez, A.L., Michael, A.C., and Cui, X.T. (2015b). Brain tissue responses to neural implants impact signal sensitivity and intervention strategies. ACS Chem. Neurosci. 6, 48–67. https://doi.org/10.1021/cn500256e.

Kozai, T.D.Y., Vazquez, A.L., Weaver, C.L., Kim, S.-G., and Cui, X.T. (2012). In vivo two-photon microscopy reveals immediate microglial reaction to implantation of microelectrode through extension of processes. J. Neural. Eng. 9, 066001. https://doi.org/10.1088/1741-2560/9/6/066001.

Kuramochi, Y., Guo, X., Sawyer, D.B., and Lim, C.C. (2006). Rapid electrical stimulation induces early activation of kinase signal transduction pathways and apoptosis in adult rat ventricular myocytes. Exp. Physiol. 91, 773–780. https://doi.org/10.1113/expphysiol.2006.033894.

Luo, X., Weaver, C.L., Zhou, D.D., Greenberg, R., and Cui, X.T. (2011). Highly stable carbon nanotube doped poly (3, 4-ethylenedioxythiophene) for chronic neural stimulation. Biomaterials 32, 5551–5557. https://doi.org/10.1016/j.biomaterials.2011.04.051.

Mahadevappa, M., Weiland, J.D., Yanai, D., Fine, I., Greenberg, R.J., and Humayun, M.S. (2005).

Perceptual thresholds and electrode impedance in three retinal prosthesis subjects. IEEE Trans. Neural Syst. Rehabil. Eng. 13, 201–206. https://doi.org/10.1109/tnsre.2005.848687.

Matsumoto, K., Sato, C., Naka, Y., Whitby, R., and Shimizu, N. (2010). Stimulation of neuronal neurite outgrowth using functionalized carbon nanotubes. Nanotechnology 21, 115101. https://doi.org/10.1088/0957-4484/21/11/115101.

Mccreery, D., Yuen, T., and Bullara, L. (2000). Chronic microstimulation in the feline ventral cochlear nucleus: physiologic and histologic effects. Hear. Res. 149, 223–238. https://doi.org/10.1016/s0378-5955(00)00190-8.

Mccreery, D.B., Agnew, W.F., Yuen, T.G.H., and Bullara, L.A. (1988). Comparison of neural damage induced by electrical stimulation with faradaic and capacitor electrodes. Ann. Biomed. Eng. 16, 463–481. https://doi.org/10.1007/bf02368010.

Mccreery, D.B., Yuen, T.G., Agnew, W.F., and Bullara, L.A. (1997). A characterization of the effects on neuronal excitability due to prolonged microstimulation with chronically implanted microelectrodes. IEEE. Trans. Biomed. Eng. 44, 931–939. https://doi.org/10.1109/10.634645.

Mortimer, J.T., Shealy, C.N., and Wheeler, C. (1970). Experimental nondestructive electrical stimulation of the brain and spinal cord. J. Neurosurg. 32, 553–559. https://doi.org/10.3171/jns.1970.32.5.0553.

Obien, M.E.J., Deligkaris, K., Bullmann, T., Bakkum, D.J., and Frey, U. (2015). Revealing neuronal function through microelectrode array recordings. Front. Neurosci. 8, 423. https://doi.org/10.3389/fnins.2014.00423.

Prasad, A., Xue, Q.-S., Sankar, V., Nishida, T., Shaw, G., Streit, W.J., and Sanchez, J.C. (2012). Comprehensive characterization and failure modes of tungsten microwire arrays in chronic neural implants. J. Neural. Eng. 9, 056015. https://doi.org/10.1088/1741-2560/9/5/056015.

Pudenz, R.H., Bullara, L.A., Jacques, S., and Hambrecht, F.T. (1975a). Electrical stimulation of the brain. III. The neural damage model. Surg. Neurol. 4, 389–400.

Pudenz, R.H., Bullara, L.A., Dru, D., Talalla, A., and TAlAllA, A. (1975b). Electrical stimulation of the brain. II. Effects on the blood-brain barrier. Surg. Neurol. 4, 265–270.

Rizzo, J.F., Wyatt, J., Loewenstein, J., Kelly, S., and Shire, D. (2003). Perceptual efficacy of electrical stimulation of human retina with a microelectrode array during short-term surgical trials. Investigative Ophthalmol. Visual Sci. 44, 5362. https://doi.org/10.1167/iovs.02-0817.

Rose, T.L., and Robblee, L.S. (1990). Electrical stimulation with Pt electrodes. VIII. Electrochemically safe charge injection limits with 0.2 ms pulses (neuronal application). IEEE (Inst. Electr. Electron. Eng.) Trans. Biomed. Eng. 37, 1118–1120. https://doi.org/10.1109/10.61038.

Salatino, J.W., Kale, A.P., and Purcell, E.K. (2019). Alterations in ion channel expression surrounding implanted microelectrode arrays in the brain. Preprint at bioRxiv. https://doi.org/10.1101/518811.

Schmidt, E.M., Bak, M.J., Hambrecht, F.T., Kufta, C.V., O'Rourke, D.K., and Vallabhanath, P. (1996). Feasibility of a visual prosthesis for the blind based on intracortical micro stimulation of the visual cortex. Brain 119, 507–522. https://doi.org/10.1093/brain/119.2.507.

Sevanian, A. (1988). Lipid peroxidation, membrane damage, and phospholipase A2 action. In Cellular Antioxidant Defense Mechanisms (CRC Press).

Staats, P., Emala, C., Simon, B., and Errico, J. (2018). Neurostimulation for asthma. Neuromodulation.

Stieger, K.C., Eles, J.R., Ludwig, K.A., and Kozai, T.D.Y. (2020). In vivo microstimulation with cathodic and anodic asymmetric waveforms modulates spatiotemporal calcium dynamics in cortical neuropil and pyramidal neurons of male mice. J. Neurosci. Res. 98, 2072–2095. https://doi.org/10.1002/jnr.24676.

Strick, P.L., and Preston, J.B. (1978). Multiple representation in the primate motor cortex. Brain. Res. 154, 366–370. https://doi.org/10.1016/0006-8993(78)90707-2.

Takahashi, S., Muramatsu, S., Nishikawa, J., Satoh, K., Murakami, S., and Tateno, T. (2019). Laminar responses in the auditory cortex using a multielectrode array substrate for simultaneous stimulation and recording. IEEJ Trans. Electr. Electron. Eng. 14, 303–311. https://doi.org/10.1002/tee.22810.

Tehovnik, E.J., Slocum, W.M., and Schiller, P.H. (2004). Microstimulation of V1 delays the execution of visually guided saccades. Eur. J. Neurosci. 20, 264–272. https://doi.org/10.1111/j.1460-9568.2004.03480.x.

Welle, C.G., Gao, Y.-R., Ye, M., Lozzi, A., Boretsky, A., Abliz, E., and Hammer, D.X. (2020). Longitudinal neural and vascular structural dynamics produced by chronic microelectrode implantation. Biomaterials 238, 119831. https://doi.org/10.1016/j.biomaterials.2020.119831.

Wellman, S.M., and Kozai, T.D. (2018). In vivo spatiotemporal dynamics of NG2 glia activity caused by neural electrode implantation. Biomaterials 164, 121–133. https://doi.org/10.1016/j.biomaterials.2018.02.037.

White, R.L., and Gross, T.J. (1974). An evaluation of the resistance to electrolysis of metals for use in biostimulation microprobes. IEEE Transact. Biomed. Eng. 21, 487–490. https://doi.org/10.1109/tbme.1974.324339.

Zheng, X.S., Yang, Q., Vazquez, A.L., and Tracy Cui, X. (2021). Imaging the efficiency of Poly(3,4-ethylenedioxythiophene) doped with acid-functionalized carbon nanotube and iridium oxide electrode coatings for microstimulatio. Adv. NanoBiomed. Res. https://doi.org/10.1002/anbr.202000092.

Yadav, A.P., Li, S., Krucoff, M.O., Lebedev, M.A., Abd-El-Barr, M.M., and Nicolelis, M.A.L. (2020). Generating artificial sensations with spinal cord stimulation in primates and rodents. Preprint at bioRxiv. https://doi.org/10.1101/2020.05.09.085647.

Yang, Q., Vazquez, A.L., and Cui, X.T. (2021). Long-term in vivo two-photon imaging of the neuroinflammatory response to intracortical implants and micro-vessel disruptions in awake mice. Biomaterials 276, 121060. https://doi.org/10.1016/j.biomaterials.2021.121060.

Yeomans, J.S., and Frankland, P.W. (1995). The acoustic startle reflex: neurons and connections. Brain Res. Rev. 21, 301–314. https://doi.org/10.1016/0165-0173(96)00004-5.

Yoo, S.-J., Ryu, S., Kim, S., Han, H.S., and Moon, C. (2017). Reference Module in Neuroscience and Biobehavioral Psychology (Elsevier).

Zheng, X.S., Tan, C., Castagnola, E., and Cui, X.T. (2021a). Electrode materials for chronic electrical microstimulation. Adv. Healthcare Mater. 10, 2100119. https://doi.org/10.1002/adhm.202100119.

Zheng, X.S., Yang, Q., Vazquez, A.L., and Tracy Cui, X. (2021b). Imaging the efficiency of poly(3, 4-ethylenedioxythiophene) doped with acid-functionalized carbon nanotube and iridium oxide electrode coatings for microstimulation. Adv. NanoBiomed Res. 1, 2000092. https://doi.org/10.1002/anbr.202000092.

## STAR★METHODS

### KEY RESOURCES TABLE

| REAGENT or RESOURCE | SOURCE | IDENTIFIER |
|---|---|---|
| **Chemicals, peptides, and recombinant proteins** | | |
| Phosphate Buffered Saline | Fisher BioReagents | BP3994 |
| 3,4-Ethylenedioxythiophene | Sigma | 483028-10G |
| Multi-Walled Carbon nanotubes | Cheap Tubes | 030106 |
| **Biological samples** | | |
| Hemizygous for Tg(Thy1-GCaMP6s) GP4.3Dkim | Jackson Laboratories | 24275 |
| **Software and algorithms** | | |
| MetaMorph | Molecular Devices | RRID: SCR_002368 |
| MATLAB | MathWorks | RRID: SCR_001622 |
| PRISM GraphPad 8 | GraphPad | RRID: SCR_002798 |
| Offline Sorter v3. | Plexon | RRID: SCR_000012 |
| NOVA 2.0 | Metrohm | N/A |
| **Other** | | |
| Ripple Grapevine System | Ripple Neuro | Nano2+Stim |
| Widefield fluorescence macroscope | Olympus | MVX-10 |
| Scanning Electron Microscopy | JOEL | JSM 6335F |
| Two-photon system | Bruker | Ultima IV |
| Ultra-fast laser | Newport Spectra-Physics | Insight X3 |
| Water immersion Lense | Nikon | 16x0.8 NA |
| Autolab Potentiostat | Metrohm | PGSTAT128N |
| DAQ board | National Instruments | PCI-6601 |
| Microelectrodes | NeuroNexus | A1x16- 5mm-703um2- 50um -CM16LP; A4x4-3mm-100-125-703-CM16LP |

## RESOURCE AVAILABILITY

### Lead contact

Further information should be directed to the lead contact, Tracy Cui (xic11@pitt.edu).

### Materials availability

No new reagents were developed in this study.

### Data and code availability

- Original data reported in this paper will be provided upon request by the lead contact.

- This paper reports no original code.

- Any additional information required to reanalyze the data reported in the paper is available from the lead contact upon request.

## EXPERIMENTAL MODEL AND SUBJECT DETAILS

### Electrode modification

Two styles of microelectrode arrays were used in this study. Four-shank probes have 4x4 iridium electrodes(A4x4-3mm-100-125-703), 3 mm long with a 125 μm shank pitch, 100 μm site spacing, and 703 μm$^2$site sizes. Single-shank (A1x16-3mm-100-703) probes have 16 electrodes of the same material and size with a site spacing of 50 μm. Before electrode surface modification each electrode site was cleaned with isopropanol and rinsed with deionized water. Activation of iridium was done by delivering voltage-controlled biphasic pulses from −0.8 V to 0.9 V at a 50% duty cycle for 3200s for each site to maximize charge storage capacity. PEDOT/CNT was prepared in 0.02M EDOT and 2 mg/mL of acid functionalized carbon nanotubes (CNTs) using chronocoulometry using our published protocols (Luo et al., 2011). To enable comparison between the two materials, the authors made every effort to ensure that the *in vitro* charge storage capacity between the two coating types showed similar values by tuning the IrOx activation parameter. These *in vitro* characterizations were reported in (Zheng et al., 2021b), where we reported the stimulation performance between the two materials in acute experiments. Specifically, when normalized by the geometric area, the charge storage capacity for PC sites 21.12 ± 0.3 and CSC for IrOx sites were 25.1 ± 1.9 (Zheng et al., 2021b). To enable within-subject comparison *in vivo*, the PC and IrOx coatings were placed on alternating sites for both electrode styles, photos of setup and electrode configurations are detailed in our previous report (Zheng et al., 2021b).

### Animal surgery

All animal work was carried out under the guidelines of the University of Pittsburgh, Institutional Animal Care and Use Committee (IACUC, protocol number 21028691, PHS Assurance Number: D16-00118). Male GCaMP6s mice (age 7-12 weeks), C57BL/6J-Tg (Thy1-GCaMP6s) GP4.5Dkim/J (also known as GP4.3) mice were purchased from the Jackson Laboratory (Bar Harbor, ME). Animals were anesthetized with 75 mg/kg ketamine and 7.5 mg/kg xylazine cocktail for cranial window surgery and electrode implantation following aseptic procedures. The electrode arrays were sterilized by ethylene oxide gas 48 hours before surgery. A reference screw was placed in the contralateral hemisphere and secured using UV-curable dental cement (# 062066 Henry Shein). A high-speed dental drill was used to remove the parietal bone over the somatosensory cortex. Electrodes were implanted at a 30° angle and inserted at a speed of 100-200 μm/s for 600 μm. Upon electrode implantation, a transparent silicone elastomer was used to seal the cranial window, covered by a 3 × 3 mm$^2$ glass coverslip. The electrode was dental cemented in place and the animal was allowed recovery and followed up with three days of analgesic and antibiotics. Due to the complexity and invasiveness of the experimental preparation, there was a sharp decline in the number of participating mice within the first two weeks of stimulation. Mice that showed poor recovery were euthanized or allowed additional recovery before stimulation. Mice that showed deterioration of cranial window clarity or whose electrodes were unfunctional were removed from the study. (Figure 4F and Table S1).

### *In vivo* imaging and electrical stimulation

This work employs the same *in vivo* imaging and electrical stimulation paradigm described previously (Zheng et al., 2021b). Briefly, images sensitive to GCaMP fluorescence over the exposed brain including the implanted electrode were acquired by widefield fluorescence imaging using a macroscope (MVX-10, Olympus, Inc.) and a high-sensitivity camera (CoolSnap HQ2, Photometrics, Inc) controlled by MetaMorph software. Time-series images were acquired at 10 Hz. In addition, images of neurons expressing GCaMP6s around the implanted electrode were acquired by two-photon microscopy (Ultima IV, Bruker Nano, Inc) coupled to an ultra-fast laser (Insight X3, Newport Spectra-Physics, Inc.) using a 16×0.8NA objective lens (Nikon, Inc.). The laser was tuned to 920 nm and time series were acquired with 1.27 × 1.27 μm/pixel resolution at 3 fps to capture GCaMP temporal responses. Imaging planes were defined as 25 μm above visible electrode contacts.

Electrical stimulation was delivered using the Ripple GrapeVine system (Nano2+stim Ripple LLC, Salt Lake City, Utah) via a 32 channel to 16 channel Omnetics adapter. The stimulation waveform was a charge-balanced cathodic leading waveform (cathodic width: 100 μs; interphase delay: 100 μs; anodic phase: 200 μs). Stimulation was delivered at 50 Hz varying the amplitude of the cathodic phase from 5μA to 60μA in the same stimulation session (the weekly timepoint). Within each session, each stimulation trial consisted of a 1-second ON period, and 3-second OFF period, repeated six times (6 trials) per electrode site,

per stimulation amplitude (5µA to 60µA), for both material types. The electrical stimulus was synced to the beginning of both imaging methods using a National Instruments board (PCI-6601, Austin, TX) to monitor the start-of-frame trigger from each system to deliver TTL pulses for each stimulation trial. The imaging and electrical stimulation were performed within 24 hours of the surgery (ascribed to the time point, day 1 or week 0) and weekly for 12 weeks. Stimulation yield is defined as the percentage of electrode sites that elicited a GCaMP response that meets the inclusion criteria for more than three stimulation intensities between 20 µA and 60 µA.

Neuronal excitability was defined as using the rheobase and chronaxie of neural elements. Strength-duration curves were generated by stimulating the brain from 1nC/ph—4nC/ph with varying pulse widths and amplitudes. The stimulation duty cycle and stimulation trials here are consistent with that performed in the mesoscale stimulation, i.e., 30s baseline followed by 1s ON and 3s OFF stimulation at each stimulation charge density, repeated 6 times. Rheobase and chronaxie were quantified by fitting the strength-duration curve of neural elements within 50 µm of the electrode center. Where rheobase represents the current at infinite pulse width and chronaxie presents the pulse width at twice the rheobase current.

## Image analysis

All image analyses were performed in MATLAB. Wide-field fluorescent time series were binned by a factor of 2 for a final resolution of 15µM/pixel to increase the signal-to-noise ratio and reduce computational load. Quantification of GCaMP response to electrical stimulation was performed on the mean of the six trials from each stimulation amplitude and stimulating electrode. Amplitude and extent of activation were extracted from the stimulation evoked responses. For this analysis, the images were cropped centered on the electrode for a final square region covering ($1.2 \times 1.2$ mm$^2$). The response amplitude (change in GCaMP fluorescence or $\Delta F/F_0$) was calculated by subtracting and dividing the mean of the initial 30 s baseline before electrical stimulation. Z-scores were calculated by dividing by the standard deviation during this baseline period. For each stimulated trial, A 2-D exponential decay function (1) was fitted to the maximum GCaMP response during the 1-second stimulation period. Where A is the amplitude of the background-subtracted GCaMP response, r is a vector representing the space of the activated region, $r_0$ represents the position of the center of the GCaMP response and w is the radius of GCaMP response. We report the amplitude and extent (radius) of stimulation-evoked GCaMP responses for those trials where the model explained at least 25% of the variance. Additionally, for instances where the GCaMP response amplitude is small or indifferent from noise, the algorithm ascribed near-flat profiles to the data with artificially large radii (w). Considering that the model can reliably capture radii (w) up to 1/3 of the half-width of the field of view, we labeled trials with GCaMP radii larger than 1/6 the width of the field-of-view as noise and excluded them from further analyses.

$$Y(r) = Ae^{-(r-r_0)/w} \qquad \text{(Equation 2-1)}$$

Efficiency measures of stimulation are quantified as neuronal activation efficiency, i.e., change in integrated GCaMP intensity per µA over 0-50 µm and 50- 100 µm; and radius efficiency, i.e., change in radius per µA. Specifically, integrated GCaMP intensity and GCaMP radius were fitted with a linear regression over the range of stimulation intensities. Stimulation sites that resulted in $p < 0.05$ for the slope of the linear fit were included in the analysis.

Neuronal expression of GCaMP across the mouse cortex is not homogeneous (Dana et al., 2014). To enable comparison between PC and IrOx in nearby but different depth locations, we normalized the GCaMP intensity and radius from PC sites to their immediate distal IrOx sites for linear arrays. For four-shank arrays, the normalization was performed by taking the ratio of PC sites to their parallel IrOx sites in the same position. For example, in 4x4 (row x column) arrangement where sites (1,1) and (1,3) are coated with PC and sites (1,2) and (1,4) are coated with IrOx, the normalizations were (1,1)/(1,3) and (1,2)/(1,4). This analysis was applied to compare both integrated GCaMP activity over 0-50 µm and 50-100 µm as well as GCaMP activation radius. Chronic comparisons of PC to IrOx were reported as the mean and standard error of PC to IrOx ratio across stimulation amplitudes 20µA–60µA. For TPM time series data, the response amplitude (change in GCaMP fluorescence or $\Delta F/F_0$) was calculated by subtracting and dividing the mean of the initial 30 s baseline before electrical stimulation.

Current amplitude for the onset of the ictal phenomenon and cortical spreading depressions were identified visually by reviewing the mesoscale time-series images. GCaMP responses accompanying ictal

phenomenon are abnormally large in amplitude and faster in pace compared to an electrically activated GCaMP response during a non-ictal state. GCaMP responses of cortical spreading depressions (CSDs) are marked by a wave of calcium signal sweeping the cortex followed by a minute of suppressed cortical calcium activity. Abnormal GCaMP responses to stimulations were removed from analyses for the longitudinal comparison between electrode materials. This was done by first removing large GCaMP responses more than a z score of 70 and removing evoked GCaMP responses more than $\pm 3$ median absolute deviations away from the mean of the GCaMP responses for each stimulation amplitude for each material.

### Electrophysiology

Neural spiking activities were acquired using Ripple Grapevine via the Nano2+Stim front end and using the Trellis software. Specifically, signal streams contain neural events that cross the threshold for a channel. The threshold is defined as 2.5 standard deviations of the spike-band-width signal. Each spike data packet consists of 52 samples captured at 30Ks/s (1.7 ms snippet) and is digitally filtered with a high pass filter of 250 Hz. Sorting of spike data was performed in Plexon offline sorter (version 3). The spike data was first sorted using the K-means automated sorting algorithm with three to five predefined clusters. The sorting results were then visually verified and incorrectly sorted units and units that consistently appeared on multiple channels (likely due to motion artifact) were discarded. Sorting was performed by the same researcher without prior knowledge of electrode mapping.

### Electrochemistry and equivalent circuit modeling

All *in vitro* measurements were performed using a three-electrode set up in PBS using Ag/AgCl as reference and Pt foil as the counter electrode. *In vitro* characterizations consisted of electrical impedance spectroscopy (EIS), cyclic voltammetry (CV), and charge injection limit (CIL). EIS was measured by applying a 10-mV signal from 10-40,000 Hz. CV was measured to calculate the charge storage capacity and to identify the electrochemical signatures of the coated materials ($-0.7$ V to 0.8 V at 1V/s scan rate). Voltage excursion was performed by bi-polar asymmetric current-based waveforms at 30 μA. From the voltage excursion, the energy for current-controlled stimulation was calculated by integrating the absolute value of the product of voltage and current over a single pulse duration (300μs ON period, 200μs cathodic phase, and 100 μs anodic phase). *In vivo* electrochemical characterization followed the same parameters as the *in vitro* setup except that a two-electrode setup was used with the reference and counter electrodes shorted to a skull screw in the contralateral cortex. All electrochemical data were collected using the Autolab potentiostat. Due to occasional instrumentation and connection errors, unrealistic measurement values were obtained and were excluded from the data analysis. Specifically, we excluded impedance measurements above 2.5 MOhm, energy measurements that were more than 40nJ, and CSC measurements outside of 3 absolute medians from the mean for each electrode coating type.

Equivalent circuit modeling was performed in MATLAB using a built-in optimization algorithm ('fminsearch'). Due to the significant low-frequency noise from *in vivo* impedance measurement, the fitting was performed in between 100 Hz – 40 kHz of the impedance spectrum. We chose the equivalent circuit model developed by Bisquert et al. (2000) which models the electrical characteristics of *in vivo* inflammatory tissue encapsulation (Duan et al., 2004). The goodness of fit was determined by visually inspecting the experimental data and the model data while ensuring less than 15% of absolute error between the experimental data and model fitting.

### Explant analysis

After the 12-week endpoint. We explanted the functional electrode arrays of two mice. Each array was first rinsed with an enzymatic cleaner (ENZOL) and DI water followed by overnight soaking in trypsin at 37°C. Electrochemical measurements after electrode cleaning were made using the same *in vitro* method described in the preceding section Electrochemistry and Equivalent circuit modeling. Scanning electron microscopy (JOEL JSM 6335F) was performed at the Center for Biological Imaging (University of Pittsburgh). The samples were cleaned with isopropyl alcohol and dried before sputter coating. To reduce charging under the electron beam, the samples were coated with a thin layer (3.5 nm) of gold.

### QUANTIFICATION AND STATISTICAL ANALYSES

All statistical analyses were performed in Graphpad PRISM 8.0. Two-way ANOVA mixed effects with Sidak's post-hoc were used for the following comparisons: The effect of time on neuronal activation intensity

efficiency for PC and IrOx coated electrodes; The effect of coating type on neuronal activation intensity efficiency. The effect of time on the radius efficiency between PC and IrOx coated electrodes; The effect of coating type on radius efficiency. The effect of distance bins away from the electrode on the ratio of integrated GCaMP intensity. The effect of time on the ratio of integrated GCAMP intensity and radius compared to 1; The effect of time on the single unit count and amplitude between PC and IrOx coated electrodes; The effect of time on the impedance, charge storage capacity, and energy between PC and IrOx coated electrodes. All sample sizes and animal numbers are denoted in their respective figure captions and supplemental information.